LHCb Collaboration LHCb 2007-103 VELO
10 July, 2007

VELO module characterisation: Results from the Glasgow LHCb VELO module burn-in

A Bates[a,*], L Dwyer[b], F Marinho[a,*], C Parkes[a], A Saavedra[a], S Viret[a]

[*] *Corresponding authors*

[a] The University of Glasgow, Dept. of Physics and Astronomy, Glasgow, G12 8QQ.
[b] University of Liverpool, Oliver Lodge Laboratory, Oxford Street, Liverpool, L69 7ZF, UK.

Abstract

The LHCb VErtex LOcator (VELO) modules were constructed at Liverpool University and assembled into the VELO detector halves at CERN. Between these two stages each module was rigorously inspected, tested and thermally cycled in the Glasgow module burn-in setup. The results of the extensive tests are summarised in this note for each one of the tested VELO modules. Major results presented in this note are the full characterisation of the leakage currents, bad channels, signal to noise measurements and metrology correlations. There were multiple small problems that were identified through visual inspections of the modules and the feed back into the production process proved critical. As a result of the electrical and thermal tests one module was withheld from production and reserved as a spare module. In addition further studies are reported which were based on individual modules such as characterisation of the timing of the front end pulse shapes.

Contents

1 Introduction

This note describes the inspection, thermal and electrical tests which were performed on the LHCb VELO modules before they were mounted onto the final VELO detector mechanics. The set-up used to perform the tests is described in detail in [1]. Details of the daily results plus documentation on the procedures are available at [2]

The note is organised as follows. The introduction below gives a brief overview of the LHCb VELO modules, their time line from production to assembly and some of the general aims of the Glasgow burn-in tests. Section 2 describes and details the procedures that were applied during each test and stage of the Glasgow burn-in measurements. Section 3 provides details on the experiment set-ups that were used for the burn-in measurements. The high resolution inspections were performed using the equipment described in Section 3.1 and details of the electrical testing set-up are given briefly in Section 3.2 and full details are provided in [1].

Sections 4 - 11 detail the results that were found for each tested VELO module in the Glasgow burn-in setup. There are eight major results sections detailed in this note. The first section, 4, documents the total number of tested modules and the inspection and testing rate. Section 5 lists the problems that were found through the detailed high resolution visual inspections. Thermal images of the modules were measured. Temperature distributions of the modules, and the change in the distributions due to the burn-in tests are described in Section 6. The signal to noise ratio measured by the front end chip header provides an estimation of the performance of the sensors on each module. A full investigation into the signal to noise ratios and the effect of the burn-in procedures upon the ratios is fully described in Section 7. For four modules the effect on the signal to noise ratio of varying the sensor bias voltage is also described.

The pre-irradiation leakage current of the sensors can highlight early problems with the modules. A full investigation of the leakage current is provided in Section 8, and Section 9 explores possible correlations between high leakage current modules and the module metrology and sensor wafer position. Section 10 characterises the pulse shapes from a standard VELO module and compares it to a VELO module with a change in sensor technology. The pulse shapes are analysed over a range of front end chip parameter settings. The final results section is Section 11 which lists the results of the electronic channels in terms of the number of bad channels for each module. Section 12 draws the conclusions from all the tests performed in the Glasgow burn-in laboratory.

1.1 VELO Modules

The LHCb VELO detector comprises of 42 modules, split into two detector halves. Each detector half is positioned only 8 mm from the nominal beam position and may be retracted up to 30 cm away during beam injection. The final VELO modules are the result of much research and are at the forefront of silicon vertexing technology. Many details of the VELO are provided in [3]. Each of the 42 VELO modules have two single sided silicon sensors glued back to back on a custom designed hybrid which contains 16 front end Beetle chips [4] on each side of the hybrid.

At the time of writing, all of the VELO modules have been produced, burned-in and assembled onto the detector halves. The next phase is the installation and commissioning of the VELO detector.

1.2 Production to Assembly

The silicon sensors were produced at MICRON Semiconductor[1] and along with all the other components, they were assembled into VELO modules at Liverpool University. Details of the assembly procedure can be found in [5]. Before each module left Liverpool it was electrically tested and sent to metrology. Each module was shipped to the burn-in laboratory which was located at CERN. The modules arrived in the burn-in laboratory in a custom built transport case which had vibration dampeners holding the module at the paddle and the hybrid and the case was filled with nitrogen [6].

Each module was extensively tested in the burn-in laboratory [1] and details of the tests are summarised in this note. After the module burn-in, each module was then hand delivered to the assembly laboratory which was also located at CERN. The module was then mounted onto the VELO detector half and underwent another electrical test. Both fully populated VELO detector halves were sent to metrology to obtain alignment constants for the start-up phase of the experiment. The detector will then be installed and commissioned in the LHCb experiment.

1.3 Burn-in

It was necessary to burn-in each of the VELO modules in an environment similar to the LHCb experiment to check for problems which could lead to module mortality. The main problems that were checked for were electrical problems, thermal stress, visual degradation or damage and any possible damage due to the transport of the module. These tests were of significant importance as they were the final testing stage before the modules were mounted on the detector halves. Once the module was permanently mounted onto the detector half it was very difficult to remove the module for inspection or debugging purposes.

2 Burn-in Procedure

2.1 Reception

The modules were unpacked from the custom built transport box and transferred to a storage box upon their arrival in the burn-in laboratory. During the transfer a checklist was followed to document the integrity of the modules upon arrival. The following items were checked by eye.

- Each module was shipped with its own uniquely fitted pair of kapton cables. For each cable the cable number was compared to the cable number in the Liverpool University database [7], the copper-beryllium kapton clamps and the connectors were inspected for damage and the cable was inspected under a grazing light to check for indents into the surface of the kapton plane or for scratches on the surface.

[1] 1 Royal Buildings, Malborough Road, Lancing, Sussex, BN15 8UN, UK

- The transport box was checked that it was still filled with nitrogen and that the box had no loose components inside.
- The module had a full low resolution inspection on the paddle, the kapton clamp connectors, the cooling face, the hybrid components, the kapton connectors, the silicon surface and the hybrid was inspected for delamination.
- A low resolution inspection with grazing light was given to the bond wires to identify any lifted bonds that may have become loose during transport.

The full reception tests and transfer to the module storage box took 30-45 minutes per module.

2.2 Visual Inspection

A high resolution inspection was given to both sides of the two sensors, hybrids and all wire bonding. The following list provides details of what was visually inspected on each module.

- The two female kapton connectors on each side of the hybrid were checked for pin alignment, debris and scraping of the pin feet.
- The surface mounted components on each side of the hybrid were inspected.
- The high voltage (HV) return lines (one line on the Φ-sensor with two sets of bond wires and two independent lines on the R-sensor where each line had two sets of bond wires).
- The scratch pads were inspected for any loose bond wires that could move during operation in vacuum.
- The surfaces of each one of the 16 front end Beetle chips on each side of the hybrid were checked for scratches, debris or any other visual problems.
- The pitch adaptors which route the silicon strips to the front end Beetle chips were checked for scratches, discolouration or debris.
- The silicon surface and the multiple floating guard rings were visually inspected for scratches, debris or stains.
- The Back End Bonds (BEB) of the Beetle chip were checked. The BEBs provide auxiliary signals such as the ground to the chip.
- The Front End Bonds (FEB) of the Beetle chip were visually inspected. The 128 FEBs were in 4 rows of 32 channels and the wire bonds connect the Beetle chip channel to the pitch adaptor.
- The Sensor End Bonds (SEB) between the silicon strip and the pitch adaptor channel were visually inspected. The SEBs were also in 4 rows of 32 channels.

Surface debris was carefully removed with nitrogen. Caution was taken not to have a flow of nitrogen perpendicular to any bond wire or to blow the debris into a region of bond wires. The visual inspection lasted between 1.5 to 3 hours for every delivered module.

After the thermal and electrical tests were performed the modules were visually inspected for a second time. During the second inspection only the BEBs, the silicon surface and the specific FEBs and SEBs that were associated with channels that had failed any part of the electrical or thermal tests were inspected. The second visual inspection lasted only 15 minutes per module.

2.3 Electrical and Thermal Tests

After the visual inspection was performed the electrical and thermal tests began. The full testing procedure that was implemented is described below. For some modules an optimised version of the procedure was used and the differences between the two procedures is also indicated below (see also section 4).The change in procedure was motivated by the performance of the first 6 modules and the required throughput of modules.

- The module was mounted into a custom built frame. The module had the 5 screws removed which are used in the LHCb experiment to secure the cooling connection. The individually matched kapton cables were connected to the hybrid and the silicon and hybrid were covered with an aluminium hood to minimise the chance of damage to the hybrid during the mounting procedures. Full procedures for handling were implemented during every module mounting and dismounting. Once mounted in the chamber, the module could be cooled, slid into the vacuum chamber, thermally imaged or electrically tested.

- Thermal images of each side of the module were taken in air with the front end Beetle chips powered and configured. During the imaging the protective hood that covers the hybrid and the silicon was removed. Approximate camera alignment procedures were established to recreate the position of the camera relative to the silicon for every module that was imaged. The purpose of the thermal analysis was to spot Beetle chips that had a high or low current consumption, and to identify regions on the silicon of high temperature. The analysis that was performed is described, along with the results in Section 6. This procedure was removed for the optimised burn-in procedures.

- Electrical data and the behaviour of the sensors leakage current were recorded in air and then again in vacuum. The procedure for taking data and measuring the leakage current is described in Section 2.3.1.

- The module was thermally cycled four times. The chiller was set to temperature extremes of -37^{o}C and +30^{o}C which approximately corresponded to hybrid temperatures of -22^{o}C and +28^{o}C, depending on the quality of the cooling connection made during the module mounting procedure. The temperature was held at each extreme for 15 minutes and the time to ramp between the extremes was approximately 20 minutes. This procedure was included in the burn-in to thermally stress the module.

- Electrical data and the leakage current behaviour were measured in vacuum only at this stage and the procedure which was followed in described in Section 2.3.1. This step was removed for the optimised burn-in procedures.
- The Beetle chips were powered and configured and the cooling was turned on. No high voltage was applied to the sensors. The module was left for a chip burn-in procedure which lasted between 16-24 hours at pressures of around 10^{-6} Torr. This test was designed to catch early chip failures.
- Electrical data and the leakage current behaviour were measured in vacuum and then in air to compare the performance after the thermal and electrical tests to the performance before. During the optimised burn-in procedure data was not taken in air, but only in vacuum. The procedure that was followed is described in Section 2.3.1.
- The module was thermally imaged again so that when the image was compared to the first image, a differential image could be created. The differential image highlighted possible areas of change during the burn-in procedure. Again, the protective hood that covers the hybrid and the silicon during the burn-in procedure was removed. The thermal imaging stages were removed for the optimised burn-in procedures.
- The module was carefully dismounted according to written procedures. During the dismounting a second visual inspection was performed.

The full procedure last around 42.5 hours if the steps were performed sequentially with no delays. The optimised procedure lasted between 29-32 hours.

2.3.1 Electrical Data and Leakage Current Measurements

Electrical data and the behaviour of the sensors leakage current were recorded either in air or in vacuum. The appropriate cooling was applied and the Beetle chips were powered and configured. The current-bias voltage relationship was measured using ramp speeds of between 0.4-0.8 Vs^{-1} and both the ramp up and ramp down were recorded. The bias voltage that was applied to the sensor in air was the larger of either 100 V or the depletion voltage as measured from capacitance - voltage measurements in Liverpool plus 50 V. The maximum bias voltage applied in vacuum was 250 V. The temperature of the hybrid was measured during the recording of the leakage current as a function of the bias voltage. When the maximum bias voltage was applied to the sensors, electronic data was recorded. The data was analysed immediately and the raw noise and the common mode corrected noise for each channel on both sides of the hybrid was plotted and a measure of the signal to noise ratio was made using the Beetle header. A list of channels which failed some set of specified cuts were listed as bad channels. There were three cuts implemented: an absolute maximum and minimum value cut of the raw noise measured in ADC counts; a maximum percentage deviation above the average common mode corrected noise calculated for a single link (a link is 32 channels); a percentage deviation below the average raw noise calculated for a single link. The list of bad channels were compared to the list of problem channels in the Liverpool database for each module. During the optimised burn-in procedure, this stage was performed only in vacuum.

3 Experimental Set-up

3.1 Visual Inspection

The high resolution visual inspections were performed using an eye-pieceless Lynx stereo dynascope with a maximum possible optical magnification of 40. Photographs were kept of all interesting areas on the modules using a 4 mega-pixel Nikon[2] CoolPix digital camera, which had a factor of 4 of optical zoom. The module was mounted in a custom built aluminium frame with perspex covers for the inspection.

3.2 Burn-in System

To fully exercise each of the LHCb VELO modules in environmental conditions which would be similar to the LHCb experiment, a burn-in system has been built and full details of the system can be found in reference [1]. To reproduce LHCb experimental conditions, the modules have to be kept in a very low pressure with the temperature of the hybrid controlled, while the electronic front end Beetle chips are operated. The burn-in system had the following main components:

- A vacuum chamber with two stage vacuum pumping system which provided pressures in the range of between atmosphere (760 Torr) and 2 - 20 $\times 10^{-6}$ Torr.
- A custom designed cooling system which provided appropriate cooling to the VELO hybrids. It facilitated temperature cycling, to thermally stress the module, and it also provided a stable temperature control of the modules when the front-end chips were exercised in vacuum.
- Low and high voltage supplies. The low voltage supply units (1 channel/hybrid) provided power to the Beetle chips (3.5 V) and the high voltage applied the bias voltage to the silicon sensors (up to 500 V).
- The burn-in data acquisition system had the capabilities to read out both sensors on a VELO module simultaneously. The system was composed of 1 Odin readout supervisor [8], 1 control board [9], 2 Tell1 boards [10] and 2 repeater boards [11]. Two dummy cards were attached to the chamber vacuum lid to connect the module inside the vacuum chamber to the repeater boards, see [1].
- Hardware interlocks. Two interlock units were used to monitor the pressure inside the vacuum chamber and the temperature of the module. In case of system malfunction, if one of these quantities passed the specified safety limits (4 x 10^{-3} Torr or 50^{o}C) the low and high voltage supplies were powered off. During the testing of all of the production modules, no interlock fired.
- To evaluate any chip failures or any changes in the module operation a FLIR[3] A40 thermal infrared camera was set up on a adapting position stage in order to capture

[2]Nikon UK Limited, 380 Richmond Road, Kingston upon Thames, Surrey, KT2 5PR

[3]FLIR Systems Ltd, 2 Kings Hill Avenue, Kings Hill, West Malling, Kent, ME19 4AQ, UK

thermal images while the chips were operated before and after burn-in. A spatial resolution of 0.7 - 1.0 mm was estimated when the plane of the module hybrid was positioned at distances of 35 - 40 cm from the thermal camera. An uncertainty on the measured temperatures of about 1°C was estimated in the temperature range of 15 - 25°C. The difference between the images of the modules before and after the burn-in was used to determine if any thermal change had occurred at any position on the hybrid and in particular on the Beetle's surface.

3.2.1 Burn-in Data Processing

The raw data acquired was received and digitised by the Tell1 boards. By means of Gigabit Ethernet cards installed on the Tell1 boards and on a Linux desktop machine the multi-event packages (MEP) were dumped and stored on a hard disk in binary file format. The binary files were processed with the VETRA package [12] and all the algorithms that were used were available on the VeloFullDataMonitor.

In the burn-in analysis there were three main algorithms which ran in sequence to get access to and then analyse the ADC and headers values which were acquired from each Tell1. The first algorithm accessed the raw ADC and headers values and organised them into histograms according to their corresponding Analogue Receiver Card (ARC), Link and Beetle chip number (0..15). The second algorithm accessed the common mode suppressed ADC and header values before and after the pedestal subtraction stage and then also saved them according to the ARC, Link and Beetle chip. The third algorithm estimated the pedestals and noise before and after the common mode suppression for even and odd events.

Common Mode Suppression

The common mode suppression was evaluated for all 2048 channels in the 16 Beetle chips for each side of the module. Each Beetle chip has 128 channels which are divided in 4 ports or links which contain 32 channels per link. The common mode suppression was calculated for each individual link. The common mode suppression calculation can be broken down into 3 steps.

1. The average ADC value ($\langle \mathrm{ADC} \rangle$) was calculated over the 32 channels on each link.

2. A new average ($\langle \mathrm{ADC}' \rangle$) was calculated excluding all channels in the link that differed significantly from the orginal average calculated in step 1. This was performed in order that the common mode suppression was not biased by strips contianing true signal pulses. $\langle \mathrm{ADC}' \rangle$ is the common mode suppression value.

3. The common mode suppressed ADC (CMSADC_i) for each channel is calculated by subtracting the common mode suppression value from the ADC of the channel i. Denoting the original ADC value of each channel as ADC_i, $\mathrm{CMSADC}_i = \mathrm{ADC}_i - \langle \mathrm{ADC}' \rangle$.

Pedestal subtraction

A pedestal map is obtained using 1000 events and the mean pedestals are subtracted afterwords. The pedestal subtraction was calculated directly on the CMSADC. It is given

by the difference between the CMSADC and the average pedestal calculated over the 32 channels in the corresponding link.

The output of the analysis algorithms were stored in a single ROOT file. All the histograms and profiles that were obtained were saved in a directory structure. This structure was used to relate the data with its respective Tell1 board. The output of the three algorithms were stored in different branches inside each of the directories.

4 Production

The VELO consists of 42 modules - 21 on each detector half. A module with the R-sensor side of the hybrid glued to the pedestal is called an R-glued (Φ-cooled) module and on the LHCb C-side detector half there were 10 R-glued modules and 11 Φ-glued modules, assembled alternately. The LHCb A-side detector half had 11 R-glued modules and 10 Φ-glued modules. 45 modules were delivered and all modules received a high resolution visual inspection and some form of electrical checks. The 45 delivered modules included 42 modules which were mounted in the VELO detector, one R-glued and one Φ-glued spare module that were not mounted on to the VELO detector halves and one Φ-glued module that was returned to the production site due to a thermal connection problem to the module.

The type of electrical testing which the module received depended on the delivery date of the module. The first 9 delivered modules were electrically tested, having their noise and leakage current measured, and were then sent to a test beam for long term running and temperature cycling. The next 6 modules underwent the full burn-in procedure which was described in section 2.3. The remaining 30 modules underwent the optimised slightly reduced burn-in procedure which was also described in section 2.3.

The dates of each module reception, visual inspection and full burn-in are shown in Figure 1. The qualification tests successfully managed to follow the module delivery rate.

5 Visual Inspections

The visual inspections of each VELO module proved to be an integral and important component of the module procedures. Section 2.2 described the details of the visual inspection procedure that was performed on every module. The following sub-sections detail just some of the interesting results from the module visual inspections.

5.1 Kapton Damage

The procedure for attaching and removing the kapton cables onto the kapton connectors on the module while applying zero force on the hybrid was performed using two tools that were designed by Liverpool University. The kapton attachment tool used a parallel force applied simultaneously to the loosely placed kapton cables on both sides of the hybrid. The removal tool has a very similar shape to a tuning fork and was used to remove one kapton cable at a time by sliding the tool along the outside of the connector and forcing the hybrid and the cable to separate. The first version of this removal tool was made of

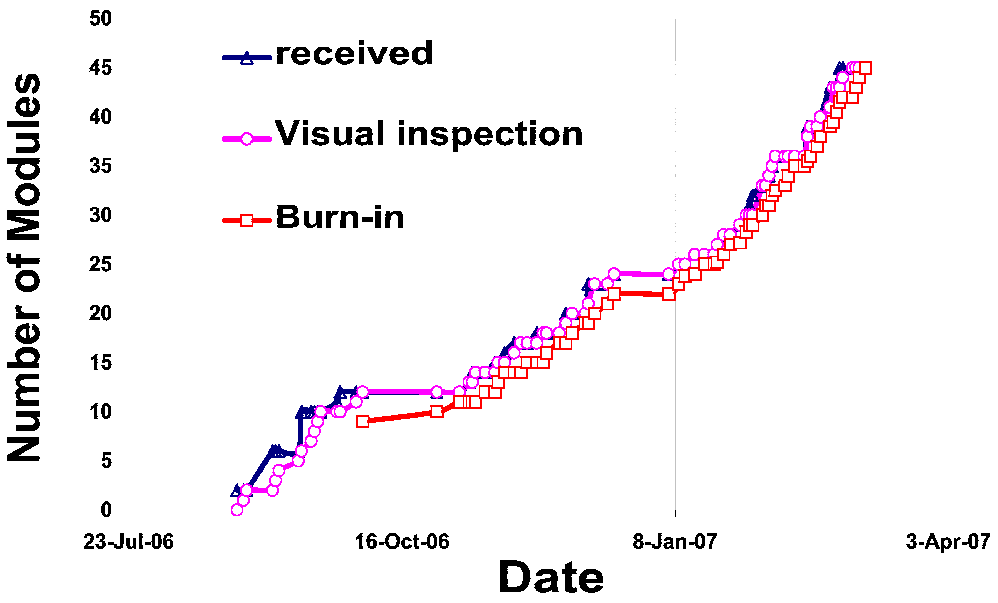

Figure 1: The dates on which the VELO modules were received, visually inspected and their burn-in completed.

aluminium and it was found during the visual inspections of the first modules that the feet on the outside of the hybrid kapton connector were being scraped and some of the feet were being broken. This was discovered early and a second version of the kapton removal tool which was made of plastic was then used. The scraping on the feet of the hybrid kapton connector was then much improved on subsequent modules.

5.2 HV Return Lines

The two HV return lines on the R-side of the hybrid and the one HV return line on the Φ-side of the hybrid were inspected on all modules (as described in section 2.2). The bond wires on some of the first modules were found to be deformed and in some cases the bonds were broken. This was traced back to a holding jig at the production site in Liverpool University. When the module was suctioned down on to the jig under vacuum, the HV return bonds which are positioned at the edge of the hybrid were being deformed by the edge of the jig. The jig was quickly altered to allow a larger opening for the hybrid to be placed on; the HV return bonds on subsequent modules were visually fine.

5.3 Silicon Surfaces

Any surface debris that was found was gently blown off with an nitrogen gun. The most common problems that were found with the silicon surfaces were small surface scratches due to production and stains from handling. The guard ring area was carefully inspected for cracks or scratches on each sensor but no problems were found.

5.4 Pitch Adaptors

The most common problems that were noted with the pitch adaptors were damage to the traces by scratches. Occasionally the scratches were deep enough to put a break in the pitch adaptor trace of a single channel. Debris was noted but not removed due to the difficult positioning of the pitch adaptors in between the FEBs and the SEBs. Surface damage like excess epoxy glue was not found to affect the electrical performance of any channels.

5.5 Bonding

Both ends of approximately half a million bonds wires have been visually inspected. There were only a small number of discrepancies between the bad channel lists that were compiled in Liverpool University by laser measurements and the visual inspection that was performed in the burn-in laboratory. The main problems that were found for the bonds were lifted bonds, electrical shorts between a few channels due to metallic debris on the SEBs and deformation in the bonds where the deformation occasionally resulted in two bonds being electrically shorted. The lifted BEBs were usually not problematic since most of the auxiliary signals were duplicated and therefore due to the redundancy in the design, the lifted bond was left. No intervention was possible in the burn-in laboratory in the case of lifted FEBs or SEBs due to the complexity of the bonding pattern. The maximum percentage of bad channels for anyone side of module was approximately 1.7 %, however, the majority of modules had much less than this value. See Section 11.2 for details of the bad channels that were electrically measured.

Two separate cases were visually found where one of the preamp bonds on the BEBs of a Beetle chip was found to be burnt and broken. Each Beetle chip has 6 preamp bonds. In each of the two cases the fragments of the burnt bonds were removed and the chip was thoroughly electrically re-tested.

6 Thermal Images

The first 6 modules which received the full burn-in procedure were thermally imaged both before and after the thermal and electrical tests. The thermal images were taken in air and with the front end Beetle chips turned on and configured. Images of each side of the hybrid which were taken before and after the burn-in were inspected for areas of non-uniformity, as was the differential image which resulted from the subtraction of the images taken before and after the burn-in procedure.

The temperature of the chiller was set to 15^{o}C and depending on the quality of the cooling connection that was achieved during the module mounting the hybrid temperature was around 34^{o}C. The temperature of the hybrid varied slightly between the thermal images taken before and after the burn-in, usually the effect was around 1-2^{o}C. An alignment procedure for the thermal camera was set-up using a well positioned jig for the thermal camera and fine alignment was performed by eye for the angular field of vision. The edge of the silicon was used as the reference for alignment. A typical misalignment was a few millimetres between objects in the thermal image of one side of the hybrid before and after the burn-in.

Figure 2 shows examples of the thermal images that were taken before and after the burn-in procedure, as well as an example of the differential image that was the result of the subtraction of the thermal images taken before and after the burn-in.

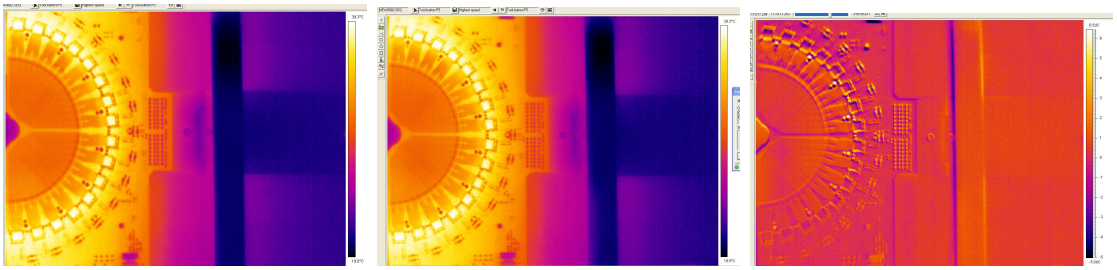

Figure 2: Three thermal images of the R-side of module 25. The silicon (the orange semicircles on the left), 16 Beetle chips (the 16 bright yellow squares positioned around the silicon), the hybrid, some of the hybrid components and the cooling block are all visible in the first two thermal images. The first thermal image was taken before the burn-in procedure and the second image was taken after the burn-in procedure. The temperature range for the first two images is between 19-39^{o}C. The third image is a pixel-by-pixel differential image between the first and second thermal images and the temperature range is between -5-6.5^{o}C.

Figure 3 shows the average temperature of each Beetle chip on the R and the Φ-hybrids of module 32 to illustrate that the Beetle chips that were positioned closest to the edge of the hybrid were slightly hotter than the middle chips since they were positioned further away from the cooling block. No irregularities were found in any of the images for all of the six modules that were imaged.

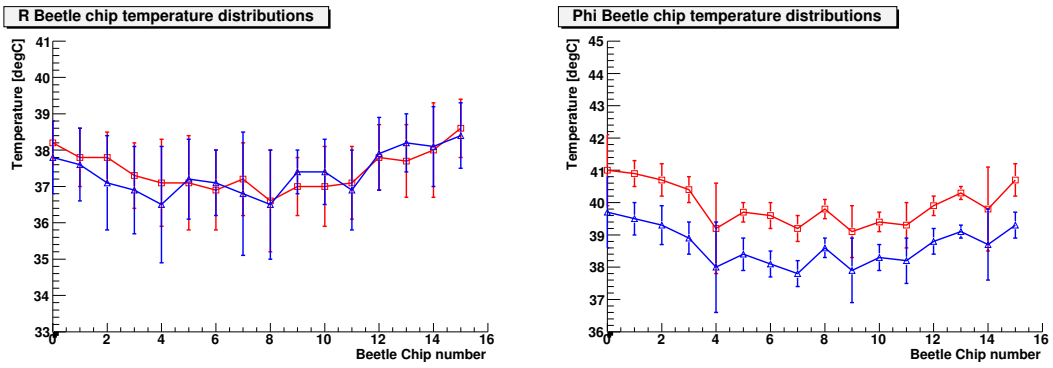

Figure 3: The average temperature of each of the 16 Beetle chips on the R (left plot) and Φ-side (right plot) of module 32. The blue triangle markers are the average temperatures before the burn in and the red squares are after the burn-in procedure. The Beetle chips are numbered sequentially from the top of the hybrid. The average temperature of the silicon on the R-side was 30.3±0.4 ^{o}C before the burn-in and 30.4±0.4 ^{o}C after the burn-in. The average temperature of the silicon on the Φ-side was 32.2±0.4 ^{o}C before the burn-in and 33.9±0.4 ^{o}C after the burn-in.

The average temperature of the Beetle chips were measured on the differential thermal

images and the distributions from the R and Φ-hybrids are shown in Figure 4. The

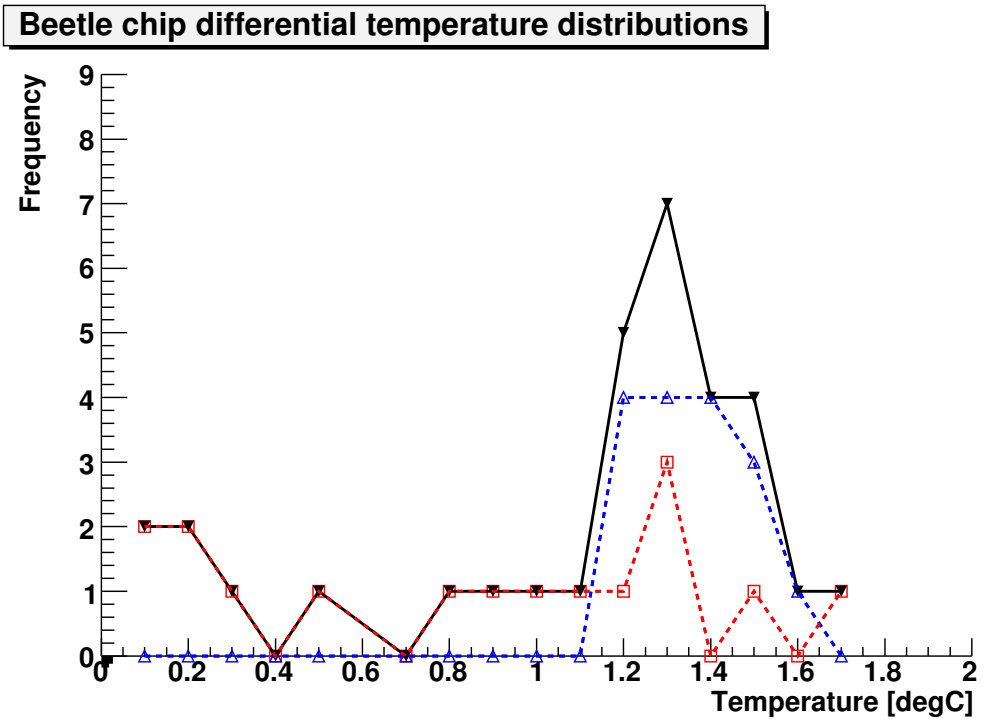

Figure 4: A histogram of the average temperature of each chip measured on the differential thermal image of before and after the burn-in procedure. The red dashed line with open red square markers shows the distribution of the 16 Beetle chips on the R-side of the hybrid and the blue dashed line with triangle markers shows the contribution from the 16 Beetle chips on the Φ-side. The black solid line shows the total for all chips on module 32.

temperature difference in each Beetle chip difference was less than 2^{o}C for all chips. Any Beetle failure that could have occurred would result in a large deviation in the chip differential temperature, however, no chips failures were detected through thermal imaging.

7 Signal to Noise Ratio

The signal to noise ratio was estimated using header signals from the Beetle. Details of the output characteristics and readout modes of the Beetle are given at [4]. The peak-to-peak header amplitude was constant over time and approximately the same for all Beetle chips. It has been verified that the amplitude of the last header bit in the analogue mode was equivalent to 3.0±0.4 times the amplitude resulting from the charge that a minimum ionising particle (MIP) would deposit in 291μm of silicon [13]. The signal to noise ratio was therefore defined by the difference of the averages of the high and low amplitudes divided by three times the average common mode suppressed noise for each link of the hybrid. All signal to noise ratio plots shown throughout this note were performed as per

the calibration given in [13]. Figure 5 shows typical plots of the noise for each of the 2048 channels on each hybrid before and after the common mode subtraction.

Figure 5 shows the noise and the common mode corrected noise as a function of both the electronic channel and the software channel. The two channel orderings differ by a rearrangement only. The capacitance of the inner and the outer strips on the Φ-sensor are different due to the difference in the strip length. This can be seen in the measured noise of the first 683 software channels of the Φ-sensor in Figure 5. The R-sensor has 4 sectors of 512 channels which increase in strip length across the 512 channels. The pattern of the 4 sectors with increasing noise can be seen in the bottom right hand plot of Figure 5.

As an illustration, the signal to noise distribution for each link on module 55 is shown in Figure 6 for both the R and the Φ-hybrids.

All of the modules that were tested in the burn-in laboratory had their signal to noise ratio estimated before and after the burn-in procedure. Figure 7 shows the signal to noise calculated for both the R and Φ-sensors as a function of the module number for the module before it was burned-in and after the module had been through the burn-in procedure. No degradation in the signal to noise was observed due to the burn-in procedure for any side of any module. The signal to noise ratio was higher for the Φ-side of the modules compared to the R-side. Figure 7 also shows the distributions for the signal to noise ratios for the modules measured before the burn-in and after the burn-in procedures.

The mean of the signal to noise distribution obtained via a Gaussian fit was the same before ($20.39 \pm 0.03 \pm 2.86$) and after ($20.44 \pm 0.03 \pm 2.87$) the burn-in procedure for the R-sensor. The first uncertainty on the means of the distributions and on the following widths come from the uncertainty in the fit and the second uncertainty comes from the calibration given in [13] for 291 μm thick silicon. The mean of the Gaussian fits to the distribution for the Φ-sensor was also relatively unchanged with a mean of $22.45 \pm 0.06 \pm 3.15$ before the burn-in and $22.37 \pm 0.06 \pm 3.14$ after the burn-in. The width of the R-sensor distributions was $0.15 \pm 0.03 \pm 0.02$ before and $0.18 \pm 0.03 \pm 0.03$ after the burn-in procedure and the width of the Gaussian fit to the Φ-sensor signal to noise ratio distribution was $0.35 \pm 0.04 \pm 0.05$ before and $0.33 \pm 0.04 \pm 0.05$ after the burn-in procedures.

7.1 High Voltage Scans

Electronic data was taken at a range of bias voltages for a few modules. The signal to noise ratio as a function of bias voltage was therefore extracted. Four modules in total were measured in such a manner and the curves obtained are shown in Figure 8. The voltage at which the signal to noise ratio starts to plateau provides an indication of the approximate point of device depletion, although this method does not provide a good accuracy in determining the depletion voltage as other methods such as measuring the charge collection efficiency.

Each of the four modules begin to plateau at bias voltages of 50 V for the R-sensors and 80 V for the Φ-sensors. Figure 9 shows the depletion voltage which was measured at Liverpool University as a function of the module number. The R-sensors of modules 38, 41, 64 and 74 all have depletion voltages between 30 - 50 V which agrees well with the signal to noise ratio voltage scans for the R-sensors shown in Figure 8. The Φ-sensors all have depletion voltages less than 80 V, which also agrees with the signal to noise ratio voltage scans for the Φ-sensors shown in Figure 8. The shape of the high voltage scans

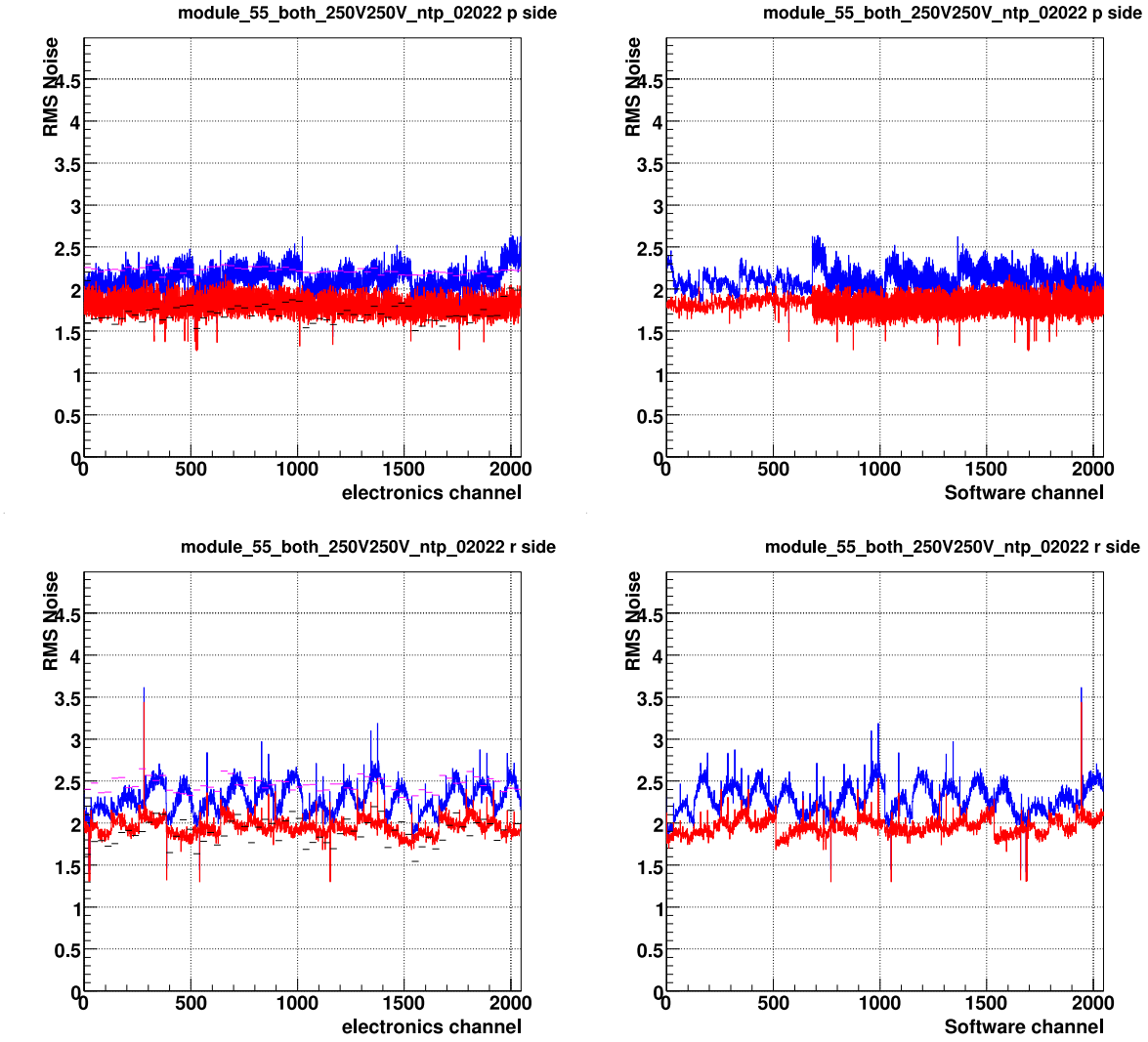

Figure 5: The top two plots shows the noise (blue) and the common mode corrected noise (red) for each channel on the Φ-side of module 55 and the bottom two plots show the noise (blue) and the common mode corrected noise (red) for the R-side of the hybrid. The two plots on the left show the noise as a function of the electronic channel and the two plots on the right side show the noise as a function of the software channel. The pink and black horizontal lines on the plots are respectively the maximum deviation of the common mode suppressed ADC values and minimum deviation of the raw ADC for each link. Full description of these analysis criteria are described in Section 11.

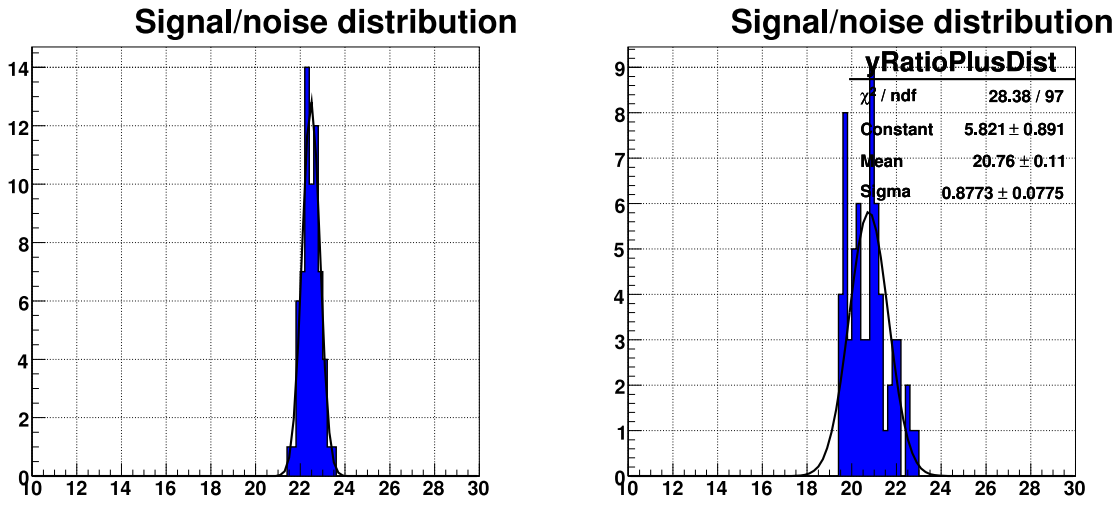

Figure 6: The signal to noise distribution per link of module 55 is shown on the left for the Φ sensor and on the right for the R-sensor.

from three of the Φ-sensors (modules 38, 64 and 74) were as expected for an n^+-in-n sensor which is read out through the segmented n^+-implants and before irradiation, see Figure 8. However, due to the low depletion voltage of the R-sensors and one of the Φ-sensors (module 41) the curves shown in Figure 8 plateau at a low bias voltage.

8 Leakage Current

8.1 Temperature Corrections

It is necessary to make temperature corrections to the leakage current measurements in order to be able to directly compare multiple measurements on one sensor, or compare modules to each other. Depending on whether the original or optimised burn-in strategy was used the number of measurements of the leakage current-bias voltage behaviour was between 2-5. Each measurement of the same module was made at a slightly different temperature. The temperature of silicon dramatically affects the leakage current. The measured current from the detector has a contribution from the bulk silicon and a contribution from the surface of the silicon. Unfortunately due to the bonding scheme of the VELO modules it was not possible to distinguish between these two contributions. The temperature dependence of the two sources of leakage current are very different. If the leakage current is dominated by the leakage of charge carriers across the band gap, E_g, of the silicon, as is the case with leakage current generation in the bulk, then the following equation can be used to scale the leakage current measured, I, at a temperature T to a reference temperature T_{ref} where k_B is the Boltzmann constant:

$$I(T_{ref}) = I(T).(\frac{T_{ref}}{T})^2.exp((\frac{-E_g}{2k_B})[\frac{1}{T_{ref}} - \frac{1}{T}]). \quad (1)$$

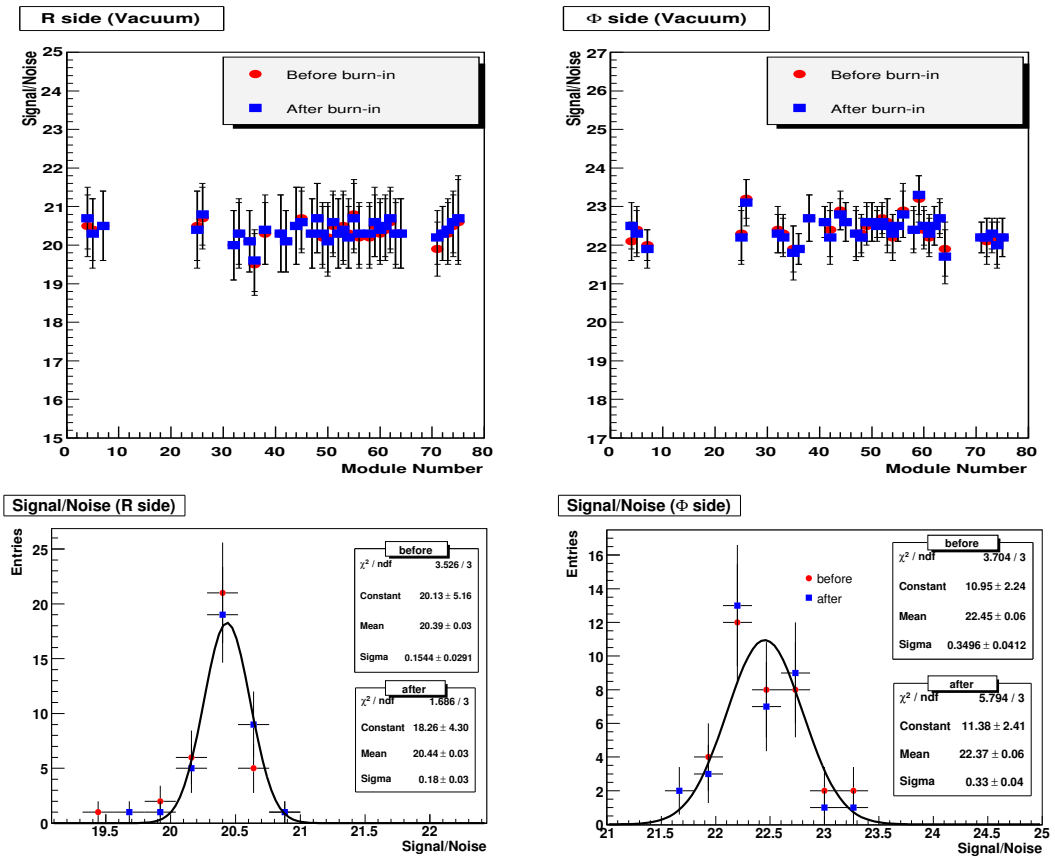

Figure 7: The top two plots show the estimated signal to noise ratio from the Beetle header as a function of the module number. The red circular markers are the measurements from before the burn-in procedure and the blue square markers are from after the burn-in procedure. The bottom two plots show the distribution of the signal to noise ratio for the measurements made before the burn-in (red circular markers) and after the burn-in (blue square markers). The Gaussian fit is shown for the fit to the signal to noise distribution after the burn-in. The plots on the left are for the R-side and the plots on the right are for the Φ-side.

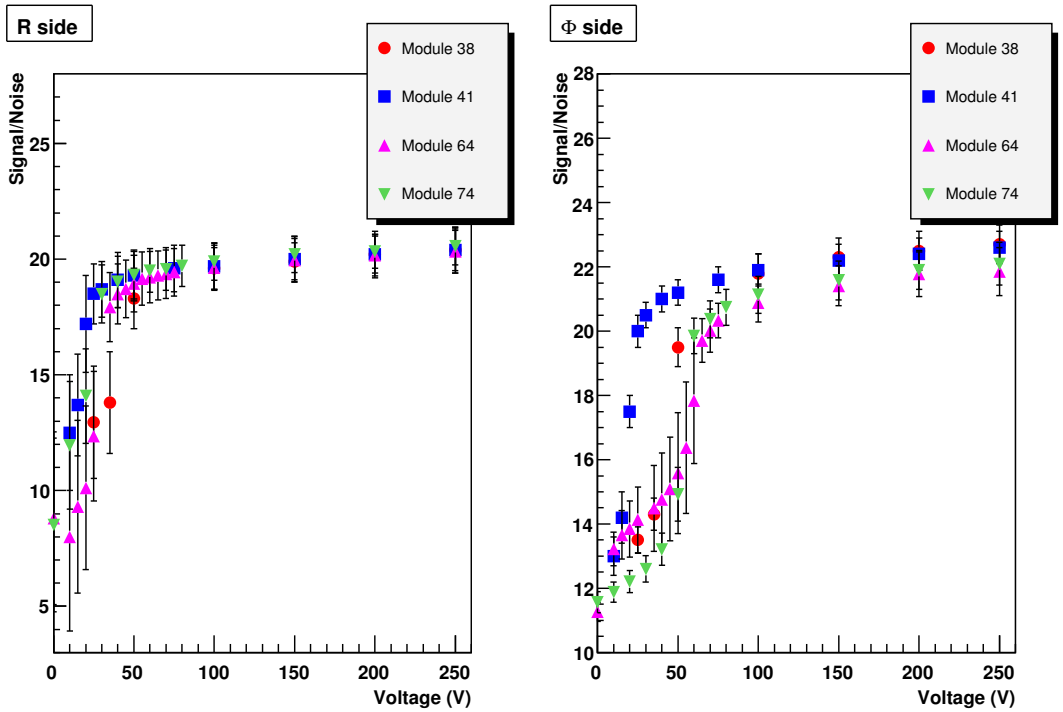

Figure 8: The signal to noise ratio as a function of the bias voltage applied on silicon sensors for the R-sensors (left) and the Φ-sensors (right).

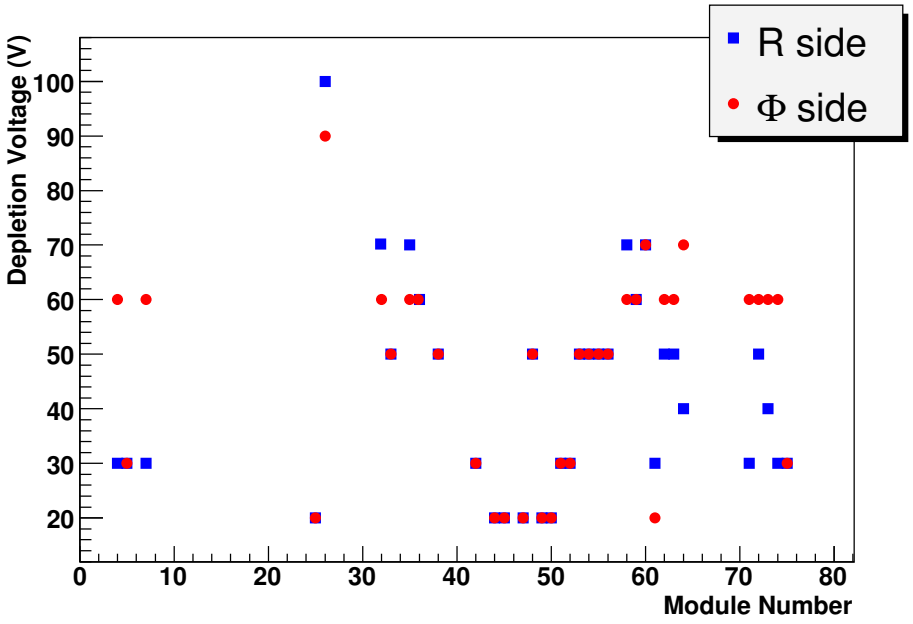

Figure 9: The depletion voltage for the R (blue square markers) and Φ-sensors (red circle markers) as a function of the module number. The depletion voltage was measured using the capacitance-voltage method in Liverpool University.

For further analysis it was useful to directly compare the numerous measured leakage currents of the sensors to each other, as well as compare the leakage current behaviour of modules to one another. Therefore, it was necessary to establish how well the leakage current obeyed Equation 1.

Two modules were studied to establish the temperature behaviour of the sensors; module 64 and module 26. Module 64 was a standard n^+-in-n production VELO module and module 26 was a production module but made with two n^+-in-p sensors. The leakage current was measured at 250 V bias on the R and the Φ-sensors while the Beetle chips were turned off. The temperature was varied using the cooling block on the hybrid and the temperature of the NTC on the hybrid was noted. Figure 10 shows the measured leakage currents as a function of the hybrid temperature.

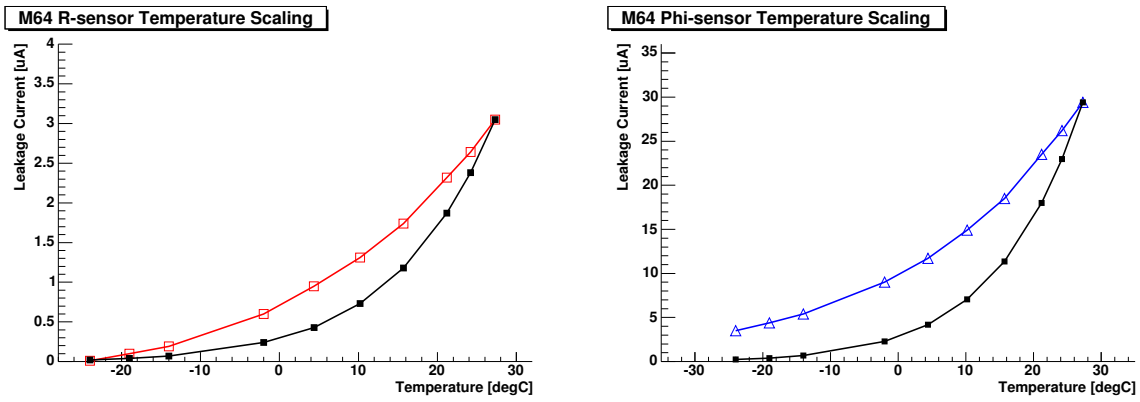

Figure 10: The temperature dependence of the leakage current measured at 250 V bias of module 64 is shown for the R-sensor leakage current on the left (red open square markers) and the Φ-sensor leakage current on the right (blue open triangle markers). The black solid square markers on both plots are the temperature scaled leakage current starting from the measured leakage current at 27.3^{o}C.

The leakage current which was measured at 27.3^{o}C was then scaled using equation 1 to the other hybrid temperatures and is compared to the measured data in Figure 10. Both the R and the Φ-sensors show an approximate agreement between the scaled and measured leakage currents.

The same procedure was performed on module 26 and Figure 11 shows the comparison between the measured and the scaled leakage currents for module 26. The measured and the scaled temperature dependence of the R-sensor of module 26 approximately agree. However, the Φ-sensor leakage current of module 26 does not agree with the temperature scaling. The leakage current of this sensor was quite high (around 50 μA) and actually decreased with increasing temperature. It can be concluded that for this sensor the leakage current was not dominated by the leakage of charge carriers across the band gap of the silicon but there must be another source of the large leakage current. Figure 12 shows the measured leakage current at 250 V bias for the Φ-sensor and indeed the leakage current was found to decrease slightly with increasing hybrid temperature.

Most of the VELO production modules were found to have leakage currents which approximately scale with temperature according to the exponential term which describes the leakage of charge carriers across the band gap. Module 26 was found to have anomalous

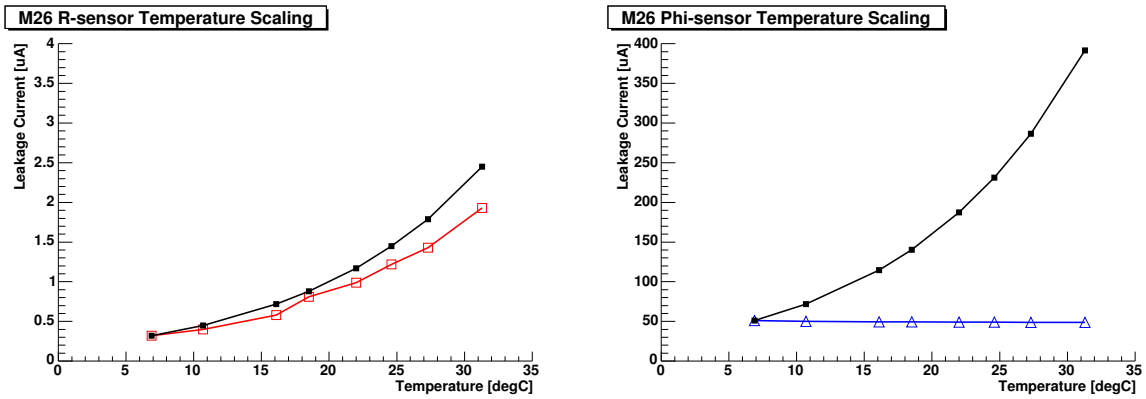

Figure 11: The temperature dependence of the leakage current measured at 250 V bias of module 26 is shown for the R-sensor leakage current on the left (red open square markers) and the Φ-sensor leakage current on the right (blue open triangle markers). The black solid square markers on both plots are the temperature scaled leakage current starting from the measured leakage current at 6.9^{o}C.

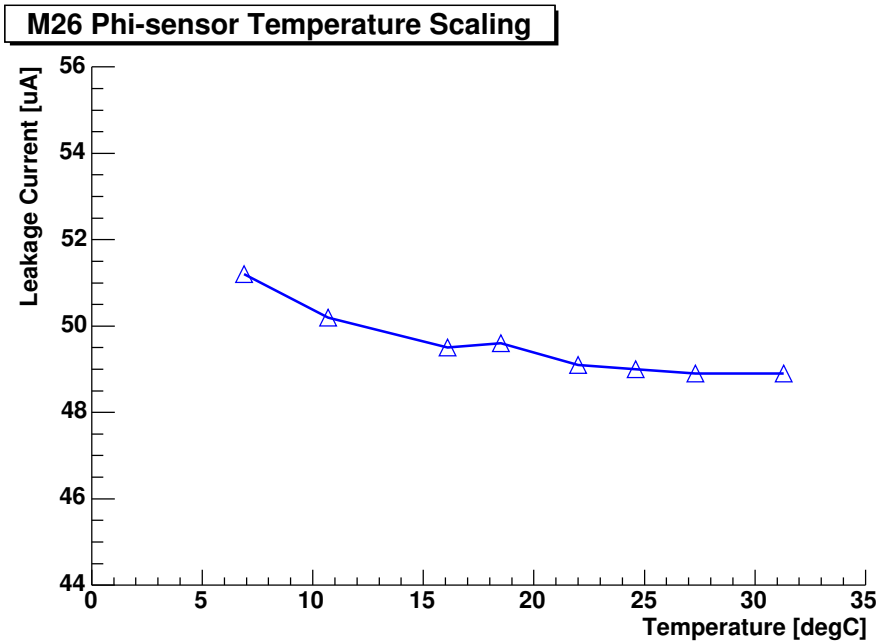

Figure 12: The temperature dependence of the leakage current measured at 250 V bias of module 26 is shown for the Φ-sensor leakage current.

leakage current behaviour, and one further sensor on module 64 was also found to behave in a similar manner which is described in Section 8.2. Therefore, two high leakage current sensors were found not to scale with temperature and furthermore, the leakage currents were found to decrease with increasing hybrid temperature. Some of the subsequent analysis in this note uses the temperature scaled leakage current. Wherever possible, both the scaled and the measured currents are provided.

8.2 Current Degradation

Measurements of the leakage current were performed on all of the VELO modules to investigate if there was any degradation in the leakage current behaviour at different stages of the burn-in tests. The leakage current was measured in Liverpool University before the transport of the modules to the burn-in laboratory, and then additional measurements were made before and after (and for some modules during) the burn-in procedure. This analysis studied the leakage current on both the R and Φ-sensors for all VELO modules.

Two basic quantities have been used to characterise the leakage current behaviour of the VELO sensors; the absolute value of the leakage current measured as a function of bias voltage and the percentage change in the measured leakage current between two stages of the production line. For the majority of the sensors the applied voltage on the silicon was 250 V, although a lower bias voltage was applied for high leakage currents (100 μA was the maximum current drawn from any sensor).

As already mentioned in the previous section, the current generated in the sensor due to the leakage of charge carriers across the band gap depends on the temperature of sensor. To compare the measured values of the sensor leakage current for many sensors or to compare the leakage current of one sensor at various measurement stages at different temperatures, it was necessary to scale them to the same temperature using the method described in section 8.1. The chosen temperature for scaling all leakage current measurements to was 20.0°C since this was the temperature when the leakage current measurements were performed in Liverpool university. Figure 13 shows the leakage measured and temperature corrected leakage currents on the R-sensors as a function of the module number. Figure 13 also shows the leakage currents which were measured at Liverpool University and just before the burn-in procedures. The percentage change in the measured and scaled leakage currents due to the difference in the Liverpool and the first burn-in laboratory measurement and due to the difference in the measurements between the leakage current measurement performed both before and after the burn-in procedure are all shown in Figure 13 for the R-sensor.

The top right hand plot in Figure 13 shows that there were no high leakage current measured on the R-sensors since all measured currents were less that 16 μA, both in Liverpool and in the burn-in laboratory. The temperatures of the silicon during the Liverpool measurements were approximately constant for all modules at 20°C, whereas the temperature of the hybrid for the burn-in measurements was highly dependent on the quality of the cooling connection that was made to the module during the mounting procedure. Therefore due to the large variation in the temperature of the burn-in laboratory measurement the centre right plot of Figure 13 shows changes in the leakage current of up to 450 % between the Liverpool and burn-in measurements. The large variation in the burn-in measurements was corrected for in the temperature scaled percentage change in the leakage current which only showed variations up to 100 %, as shown on the middle left plot of Figure 13. As expected for this plot the overall spread was around zero, however, since the absolute values of the measured leakage currents were small (less that 16 μA for all sensors but most of the sensors were measured to draw less than 5 μA) a percentage change of 100 % in the current does not indicate any unexpected behaviour or large degradation in the sensor performance. The percentage change in the leakage current measured before and after the burn-in procedure was within ±100 % for all R-sensors and

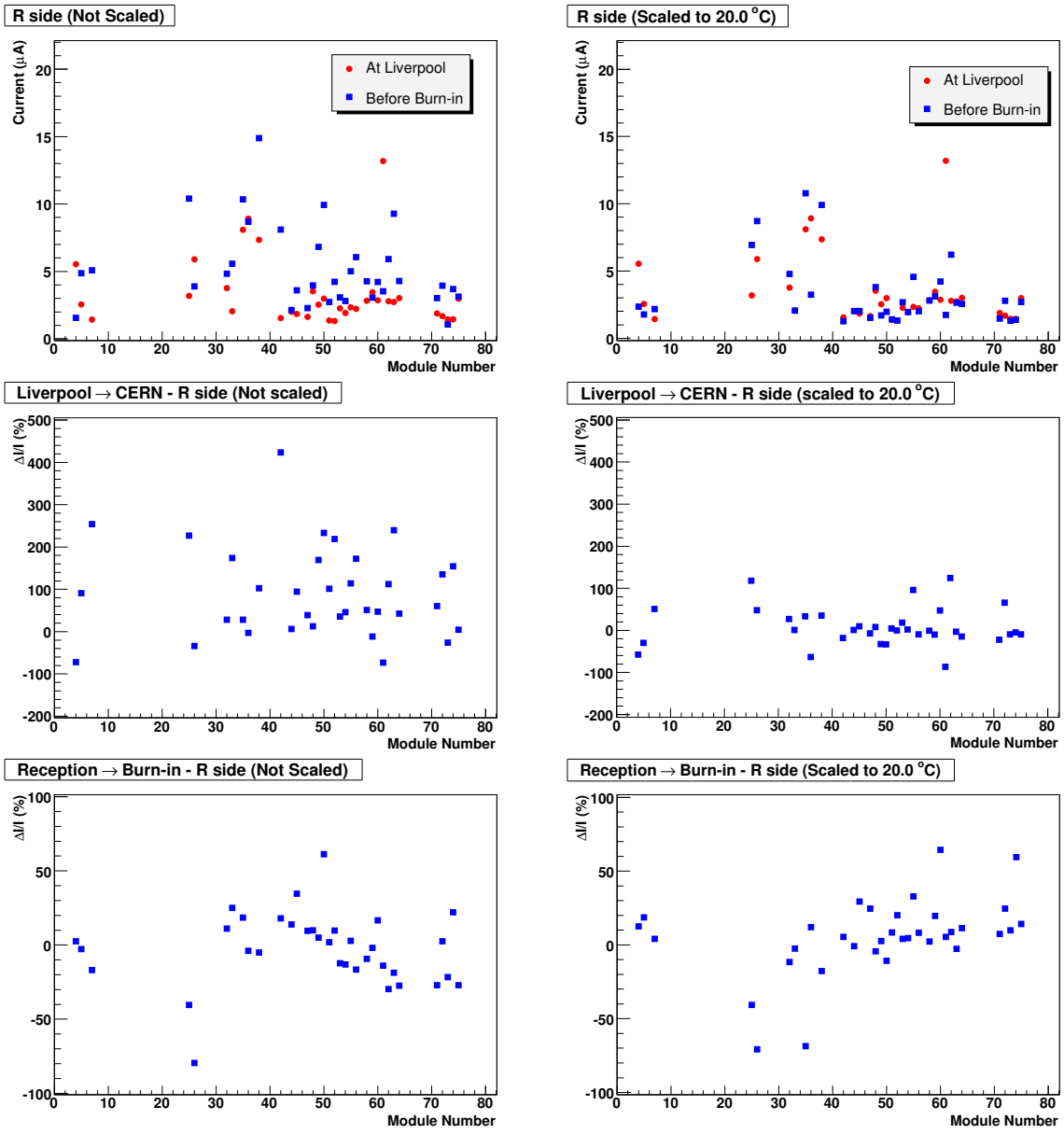

Figure 13: The top two plots show the measured (left plot) and temperature scaled (right plot) leakage current as a function of VELO module number for the R-sensors. The leakage current measured in Liverpool are the red circle markers and the leakage current measurements performed in the burn-in laboratory before the burn-in procedure is shown by the blue square markers. The middle two plots show the percentage change in the measured (left plot) and temperature scaled (right plot) leakage current between the measurements made in Liverpool University and before the burn-in procedure. The bottom two plots show the percentage change in the measured (left plot) and temperature scaled (right plot) leakage current between the measurements made before and after the burn-in procedures. The plots of the leakage currents were scaled to 20.0 ^{o}C.

the temperature corrected changes were similar since the measurements performed before and after the burn-in were performed at very similar hybrid temperatures. The bottom right plot of Figure 13 shows that for the majority of the R-sensors the leakage current increased slightly after all of the burn-in tests.

The analogous plots for the Φ-sensors are shown in Figure 14. The top left plot in Figure 14 shows some sensors with high leakage current measurements (40 - 100 μA). As mentioned in section 8.1 the leakage current on some high leakage current sensors do not obey the scaling law. The Φ-sensor on module 26 was measured to be one such sensor and therefore its temperature corrected leakage current does not follow the scaling law and the large current shown for module 26 on the scaled plot on the top left plot of Figure 14 is nonsensical. Modules 35 and 36 also show high leakage currents. The measured current for module 35 at Liverpool and before the burn-in are quite similar, hence the middle right plot of Figure 14 shows a small percentage change in the leakage current. Module 36 was one of the very few cases where the measured current before the burn-in procedure was lower than the current which was measured at Liverpool University. The two plots on the bottom row of Figure 14 shows that the leakage current of modules 35 and 36 decreased between the measurements made before and after the burn-in procedures, which was in contrast to the slight increase in the leakage current that was measured for most of the Φ-sensors during the burn-in procedures.

Modules 61 and 64 showed a significant increase in leakage current between the measurement made at Liverpool University and the first burn-in measurement, see the middle left plot in Figure 14, but the absolute values for the sensor currents are lower than 20 μA. The Φ-sensor of module 64 showed an increase of 1000 % in the measured leakage currents in Liverpool and the burn-in laboratory and an increase of 600 % in the temperature scaled leakage current. Due to these large degradations in leakage current, module 64 was withheld from the normal production and re-tested. The leakage current was measured after the burn-in procedure at 10 different hybrid temperatures over the range of 7 - 32^{o}C, while the Beetle chips were not operated, see the left plot on Figure 10. The module was then temperature cycled 3 times between +30^{o}C and -37^{o}C and then the leakage current was remeasured at three different hybrid temperatures with the Beetle chips turned off. The module was then thermally cycled a third time for two cycles between +30^{o}C and -37^{o}C and then the leakage current was remeasured at four different hybrid temperatures with the Beetle chips turned off. The leakage currents which were measured after each thermal cycle are shown in Figure 15.

Figure 15 shows that the Φ-sensor of module 64 showed no further degradation in the leakage current with subsequent thermal cycles. For safety the module was kept as a spare module and not used as a production module.

Module 75 showed a 50 % increase in the temperature scaled leakage current shown on the bottom right plot of Figure 14. Figure 16 shows the current measured on the Φ-sensor of module 75 for three different temperatures and it does not scale as expected using equation 1. The leakage current was measured to be constant over an 8^{o}C temperature range, see Figure 16, therefore the leakage current of the Φ-sensor of module 75 is the second example of a sensor which did not scale with temperature. Therefore the scaled graphs cannot be considered as a correct representation of the leakage current for this sensor. This module was mounted in the final VELO detector.

In summary, the leakage current of all of the R and Φ-sensors have been investigated at Liverpool University and before and after the burn-in procedure. The R-sensors behaved

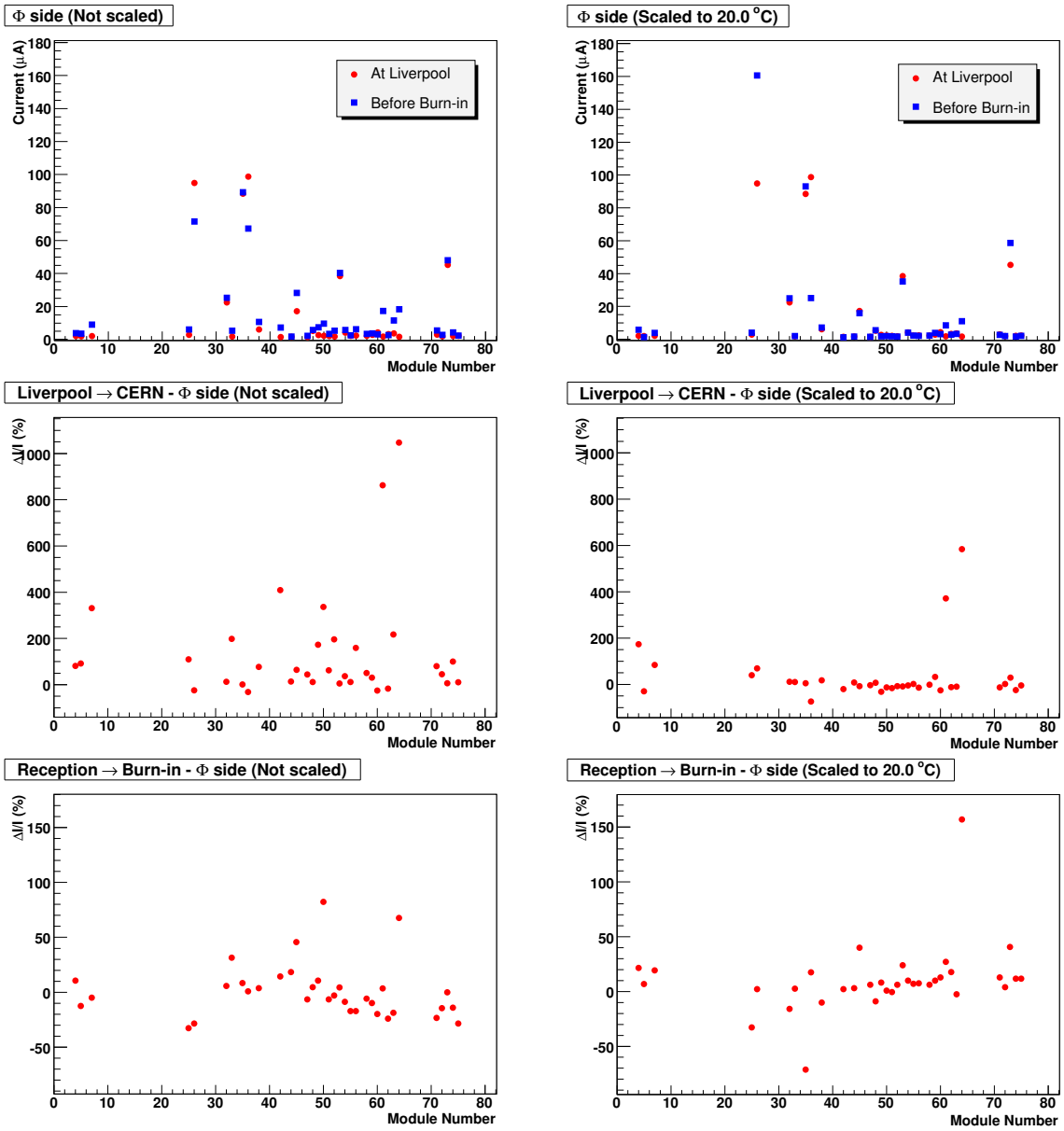

Figure 14: The top two plots show the measured (left plot) and temperature scaled (right plot) leakage current as a function of VELO module number for the Φ-sensors. The leakage current measured in Liverpool are the red circle markers and the leakage current measurements performed in the burn-in laboratory before the burn-in procedure is shown by the blue square markers. The middle two plots show the percentage change in the measured (left plot) and temperature scaled (right plot) leakage current between the measurements made in Liverpool University and before the burn-in procedure. The bottom two plots show the percentage change in the measured (left plot) and temperature scaled (right plot) leakage current between the measurements made before and after the burn-in procedures. The plots of the leakage currents were scaled to 20.0 ^{o}C.

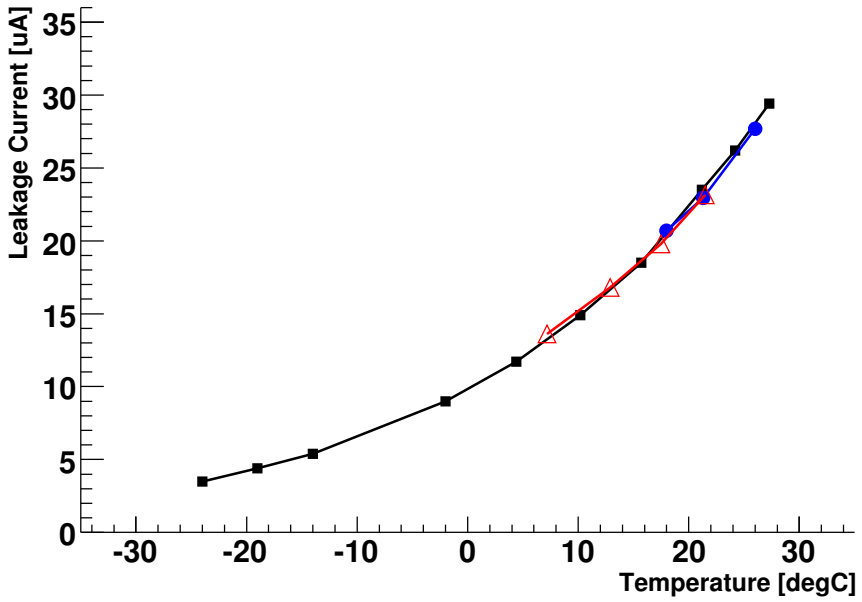

Figure 15: The temperature dependence of the leakage current measured at 250 V bias of module 64 is shown for Φ-sensor leakage current. The leakage current measured after the standard burn-in thermal cycle (4 cycles) are shown with the black solid square markers. The leakage current measured after a second thermal cycle (3 cycles) are shown in the blue solid circles. The leakage current measured after a third thermal cycle (2 cycles) is shown in the red empty triangles.

well and most of the sensors had a leakage current less that 16 μA and only changes of around 50 % due to any two consecutive measurements. The Φ-sensors contained a few high leakage current sensors. The Φ-sensor of module 26 and module 75 were found not to scale according to the expected temperature dependence. Only a few Φ-sensors showed degradation in the leakage currents but after further tests on these sensors, only one module was not used for production and was held as a spare.

9 Metrology

As discussed in the previous section, a few modules have shown a higher than normal leakage current on the Φ-side. In some cases it was detected before the burn-in procedures began but in some cases the current increased during the electrical and thermal tests. To test if the increment in the leakage current was correlated with any mechanical stress in the module a correlation study with the Liverpool metrology measurements was performed.

Four different sets of variables were investigated. The first set was a collection of measurements made of the sensors with respect to the baseline or Liverpool metrology reference frame. Table 1 shows all the variables that were used and their respective definitions according to the Liverpool database.

Figures 17 and 18 show the distribution of the metrology parameters as a function

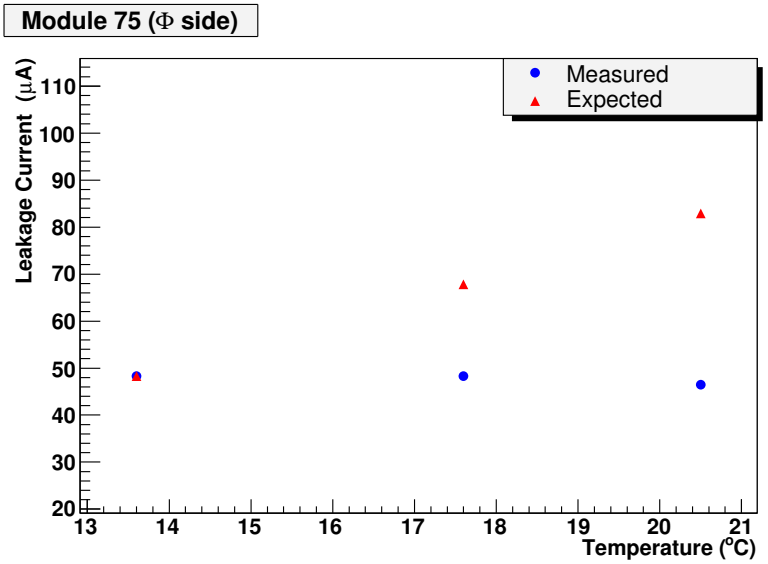

Figure 16: The measured (blue circle markers) and temperature scaled (red triangle markers) leakage current measured on Φ-sensor of module 75 for 3 different temperatures.

Table 1: Module metrology parameters

Parameter	Definition
Twist	Rotation on x axis (mrad)
Tilt	Rotation on y axis (mrad)
Z maximum	Maximum z on top of the module (mm)
Z minimum	Maximum z on top of the module (mm)
Tilt 1	Top module displacement wrt baseline at initial Metrology (mm)
Tilt 2	after cabling (mm)
Tilt 3	after tests without cabling (mm)

Table 2: Sensor metrology parameters

Parameter	Definition
Rotation	Sensor rotation wrt frame (mrad)
X shift	Sensor X shift wrt frame (mm)
Y shift	Sensor Y shift wrt frame (mm)
Total shift	Sensor total shift wrt frame (mm)
Sagitta	Maximum surface dist to reference plane (mm)

of the leakage current and the percentage change in the temperature normalised leakage current. Both Figures show the temperature normalised current versus the metrology variables in the left column. The right column shows the change in the percentage of the leakage current due to the thermal and electrical tests as function of the metrology parameters. The red circles were the modules which presented either high leakage current levels or large increases during the burn-in procedures. No correlation has been identified with any of the module parameters

The second set of metrology variables that were investigated were the contour shape measurements of the sensors. Table 2 lists all the parameters from the contour and surface measurements that were used. During the Liverpool metrology there were two different fits that were performed to evaluate the contour of the sensors. In the first fit the measurements are done with respect to the fiducial on the silicon and in the second fit the metrology measurements are compared to a reference frame which sits on the centre position of the sensor. A total of 20 positions were measured on the Φ-sensors and were compared to an ideal module. The statistical results on the residuals for each position were also analysed. Figure 19 shows the plots of the parameters from the sensor shape fit and Figure 20 shows some of the plots obtained from four examplepositions on the sensor. All the 20 postions on each Φ-sensor were measured in Liverpool University and 160 similar plots to the ones shown in Figure 20 were done in order to uncover any possible correlations. No conclusive information was extracted since the high leakage current modules had at the worst case one of these statistical quantities values located just on the edge of the distribution and not considerably displaced with respect to the other points. No correlation was identified between the leakage current and the sensor metrology parameters.

The third set of metrology variables that were investigated were the curvatures of the sensors. The sensor curvature was evaluated by comparing the fit of the sensor surface to a reference plane. The sagitta extracted was used in the correlation studies. Again, there was no explicit dependency between the higher current sensors and their sagitta values, as can be seen in Figure 21.

The fourth set of metrology variables that were investigated were the positions of the silicon on the wafers during manufacturing. Two different mask sets were produced, one for Φ-sensors the other for R-sensors. The Φ-sensor mask sets allowed for the fabrication of 3 sensors per wafer (labelled A,B,C). The R-sensor mask set had only 2 sensors per wafer (labelled D,E). Figure 22 clearly shows that all the modules with higher current levels (red circular markers) were in wafer position A, with the sole exception of module 64

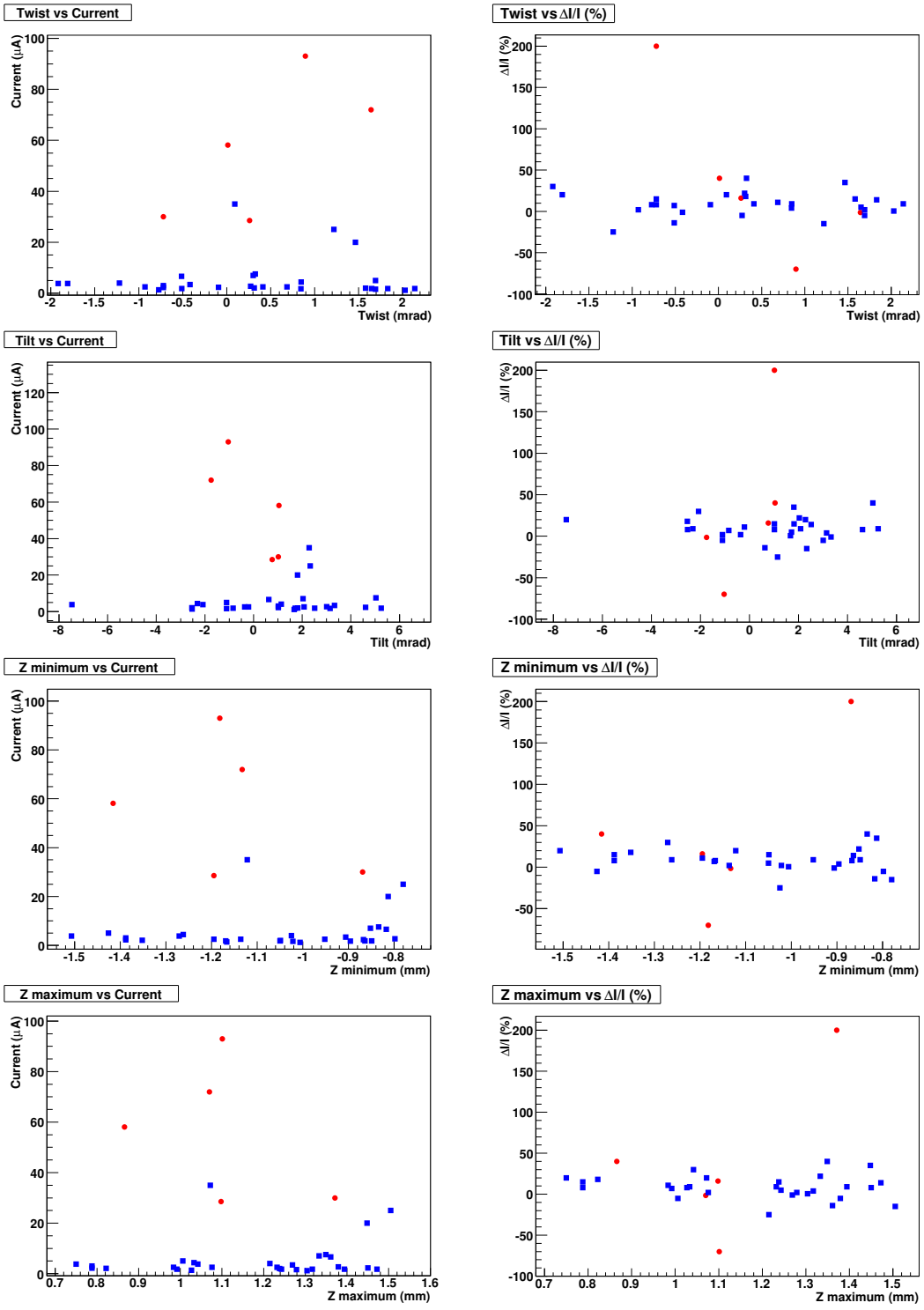

Figure 17: The left column shows the leakage current versus the various metrology parameters. The right column shows the percentage change in the leakage current due to the burn-in procedure as a function of the metrology parameters. The red circles are the modules which have either a high leakage current or a large increase in current during the burn-in procedures. No correlation was found between the higher leakage current sensors and the module metrology parameters.

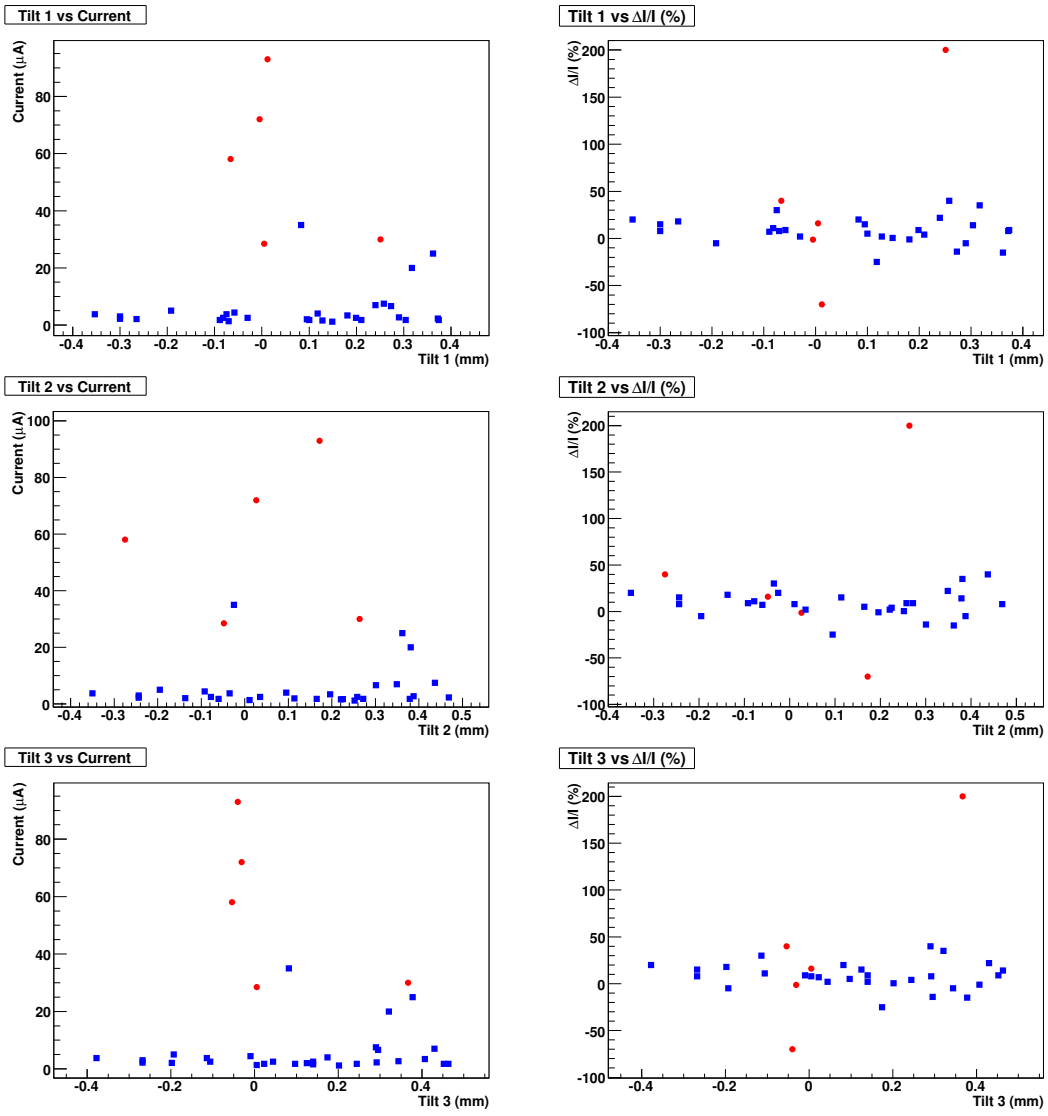

Figure 18: The left column shows the leakage current versus the various metrology parameters. The right column shows the percentage change in the leakage current due to the burn-in procedure as a function of the metrology parameters. The red circles are the modules which have either a high leakage current or a large increase in current during the burn-in procedures. No correlation was found between the higher leakage current sensors and the module metrology parameters.

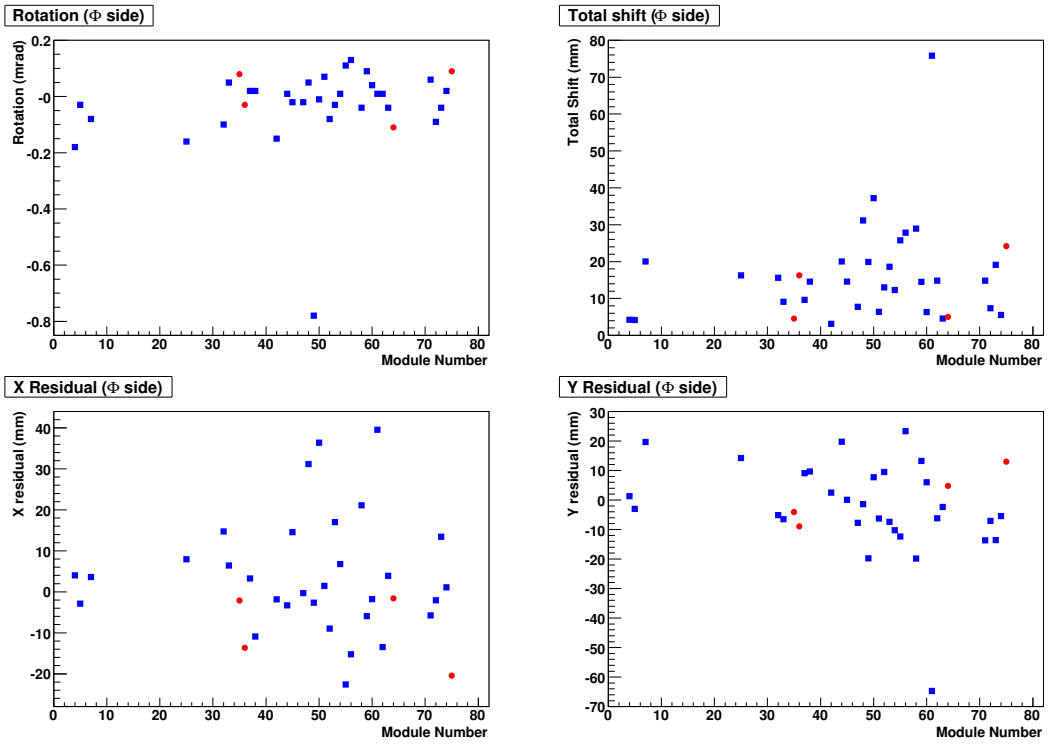

Figure 19: Each plot shows one of the first four sensor metrology variables listed in Table 2 as a function of the module number. The red circles are the modules which have either a high leakage current or a large increase in current during the burn-in procedures. No correlation with the shape fit parameters has been observed.

which was in position B on the same wafer. Sensors from B and C positions on the Φ-wafer faced each other, almost making a circle. This was the same layout for the R-sensors where the D and E positions were facing each other, almost completing a circle. Position A on the Φ-sensor was placed vertically beside positions B and C, and Figure 22 shows that all high leakage current sensors except one were from wafer position A.

Figure 23 shows the measured leakage current as a function of the date of the first leakage current test in Liverpool. It shows that the high leakage current sensors were not tested during the same period. Therefore the high current can not be associated to a particular fault that may have occurred during a specific short period of time.

So in conclusion, there were no correlations found between the modules with a high leakage current and any of the 3 sets of metrology variables that were studied. The only correlation that was found was that the majority of the high leakage current sensors were found to come from the wafer position A during manufacturing.

10 Pulse Shape Studies

Data was taken using test pulses with VELO modules in order to evaluate the characteristics of the Beetle chip parameters and to compare the response of n^+-in-n and n^+-in-p VELO modules. The test pulse signal height and the *overspill* were extracted from the

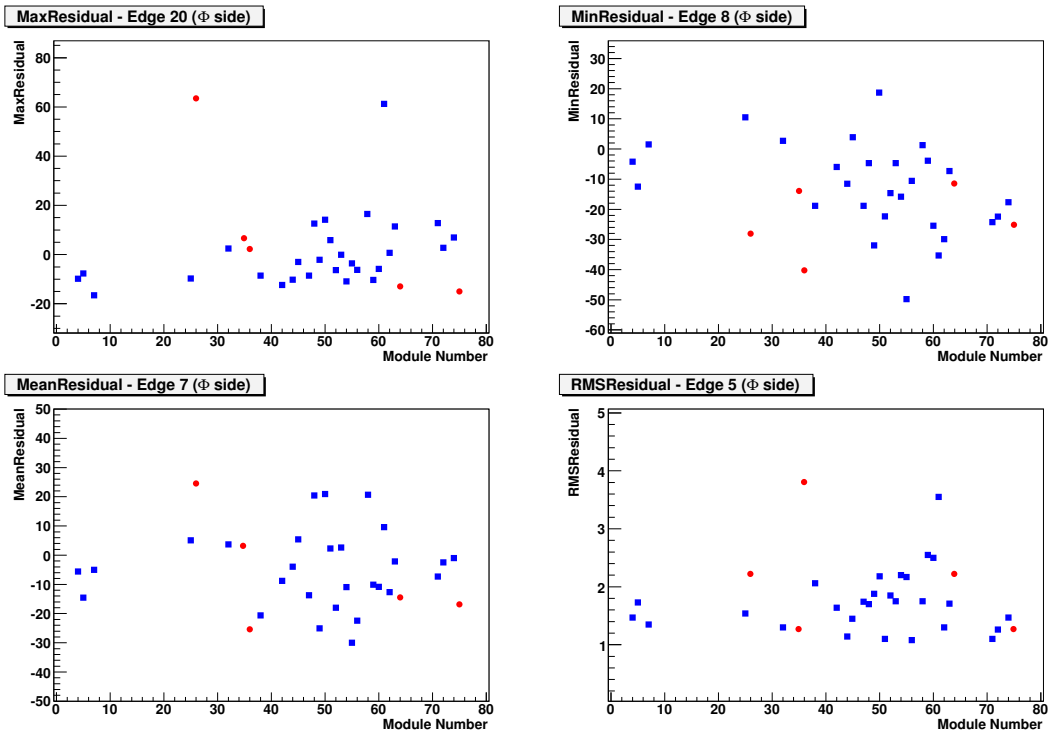

Figure 20: The maximum residual (top left), the mean residual (bottom left), the minimum residual (top right) and the RMS of the residual (bottom right) as a function of the module number for four different positions measured on the sensors. The red circle markers are the modules which have either a high leakage current or a large increase in current during the burn-in procedures and the blue square markers were measured to have a normal leakage current behaviour. For further details see text.

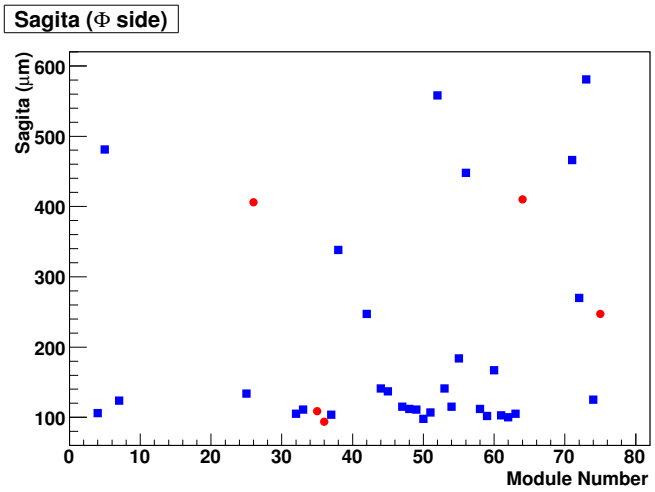

Figure 21: The sagitta of the sensor as function of the module number. The red circles are the modules which have either a high leakage current or a large increase in current during the burn-in procedures.

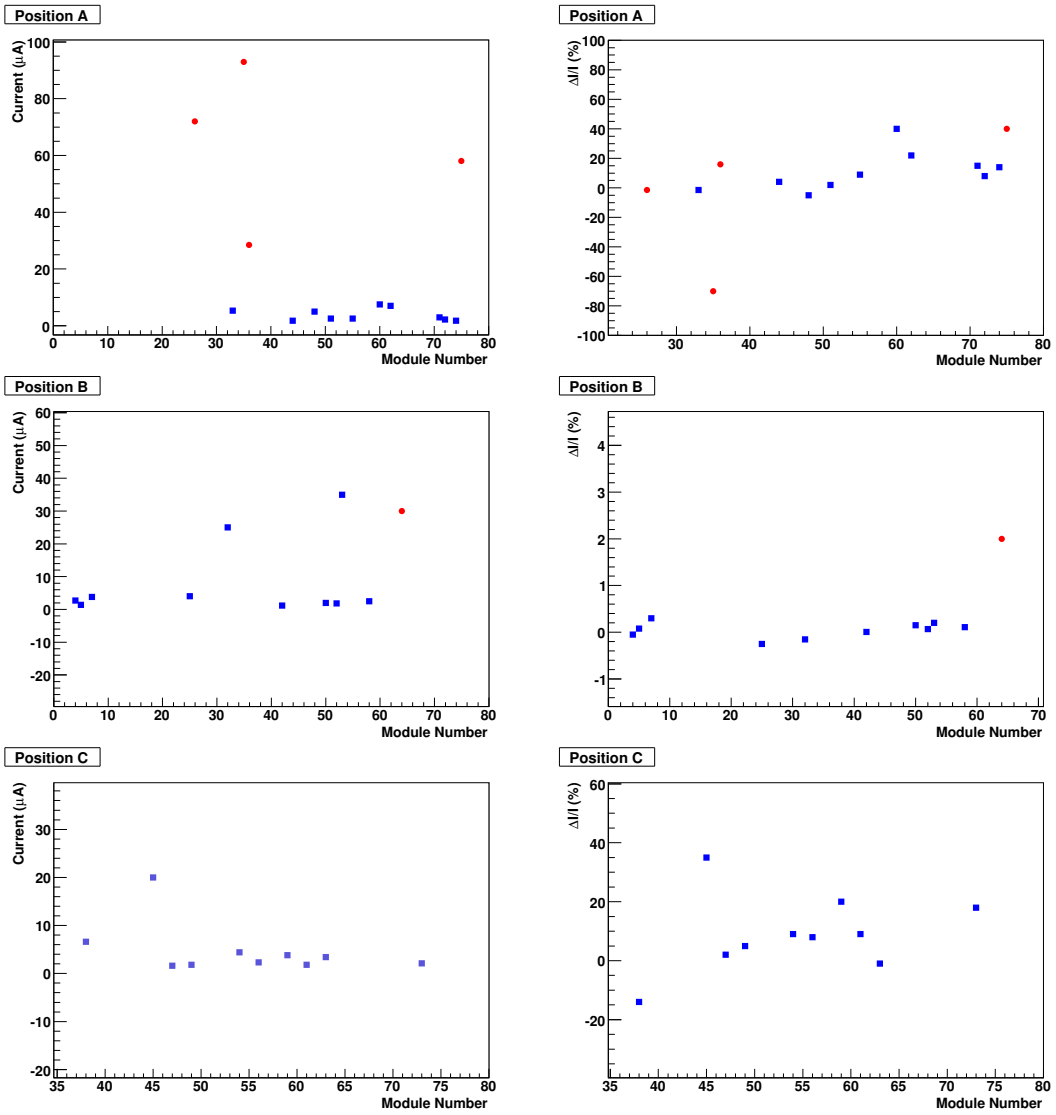

Figure 22: Each plot on the left hand column shows the temperature normalised leakage current as a function of the module number for each of the 3 Φ-wafer positions. The right hand column shows the same plot with the vertical axis showing the percentage change in the leakage current due to the thermal and electrical tests. The red circles are the modules which have presented either a high leakage current or a large increase in current during the burn-in procedures. Most modules with higher currents were in position A with just one module in wafer position B.

sets of data taken with different values for various Beetle chip parameters. The *overspill* is defined as the pulse amplitude at 25 ns after the pulse peak.

A detailed description of the Beetle chip and its relevant parameters can be obtained from [4] and a further explanation of the Beetle parameters can also be found in [14]. The following Beetle parameters were analysed:

- Pre-amplifier feedback voltage (V_{fp}): The effect of V_{fp} is seen on the undershoot region of the pulse shape. The maximum undershoot reduces and restoration is

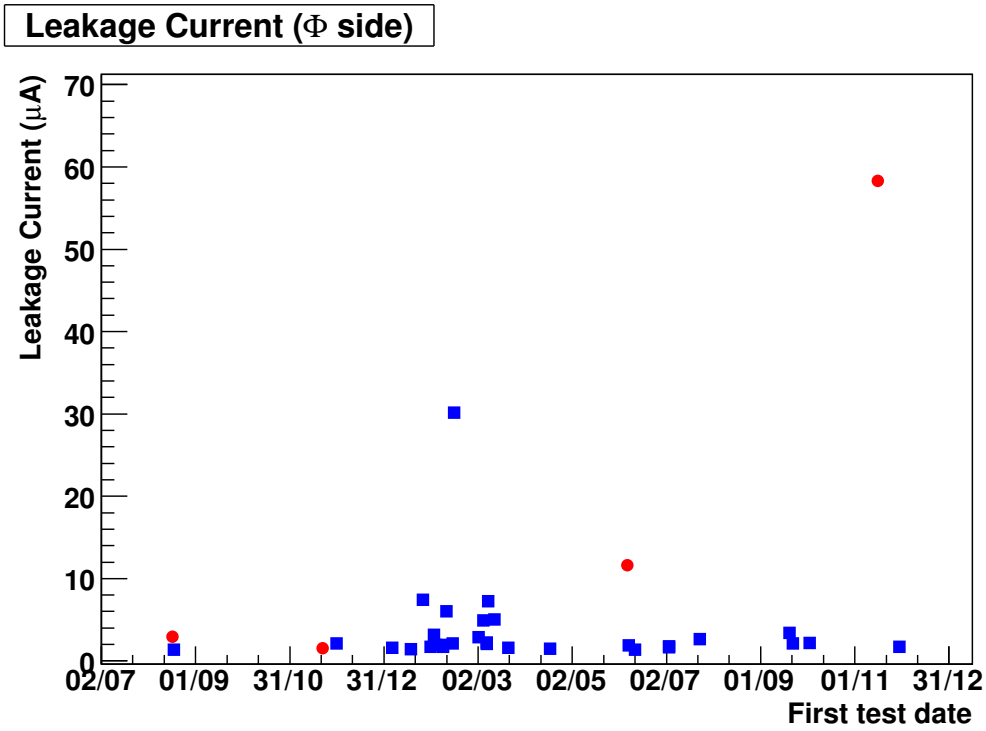

Figure 23: Leakage current of the Φ-sensors as a function of the date of the first leakage current measurement at Liverpool University. The red circles were the modules which presented either high leakage current levels or large increases during the burn-in procedures and all other modules are shown with blue square markers.

faster as V_{fp} increases.

- Shaper amplifier feedback voltage (V_{fs}): An increase in V_{fs} results in longer rise-times, higher peak signals and increased overspill.
- Pre-amplifier bias current (I_{pre}): The rise time and fall time of the signal reduces when I_{pre} is increased. Hence it reduces the overspill and increases the undershoot.
- Shaper amplifier bias current (I_{sha}): An increase in I_{sha} reduces the rise-time and undershoot.

The default values for the Beetle parameters that were used in the standard burn-in laboratory measurements, as well as the additional values used in the tests are listed in Table 3. The default parameters that are used for the Beetle chip in the LHCb experiment are 200 mV and 550 mV for the V_{fp} and V_{fs} parameters respectively, which are unfortunately outside the range of parameters tested in this note.

Figure 24 shows the test pulse shape on the electronic channel 23 on the first link of the first Beetle chip (chip 0). It was done for the n^+-in-p and n^+-in-n modules on both the R and Φ-sides of each of the two VELO modules. These plots were obtained by performing a Gaussian fit to the data in each time slice and extracting the mean of the fit. The errors of the mean were of the order of 0.1. The uncertainties shown in the plots were the sigmas obtained from the fit. The default Beetle chip parameters were used to

Table 3: The standard values and the tested set of Beetle chip parameters.

Parameter	Definition	Default	Other tested values
V_{fp} (mV)	Pre-amplifier feedback voltage	0	20, 40
V_{fs} (mV)	Shaper feedback voltage	700	600, 650, 750, 800
I_{pre} (μA)	Pre-amplifier bias current	600	400, 800
I_{sha} (μA)	Shaper bias current	80	120, 150

make this comparison. Apart from the signal height, no considerable differences on the characteristics of the pulse shapes were observed. The difference in the test pulse peak signal between n^+-in-n and n^+-in-p technologies was measured to be 6.7±0.5 % with a sigma of 3.2±0.5 on the R-side and 6.9±0.4 % with a sigma of 3.1±0.3 on the Φ-side using the default Beetle chip configuration. These numbers were obtained through averaging over a total of 64 channels per sensor. Four channels were pulsed on each Beetle chip. One chip has 4 links and one single channel was pulsed per link.

Figures 25, 26, 27 and 28 show the test pulse shapes for the studied configurations of chip parameters. In each of these Figures, only one of the chip parameters was changed while the others are set to the default values.

A 6th order polynomial was fitted to the test pulse shape in a time range of 80 ns to obtain the signal peak and estimate the overspill. The range was set so that the lower limit was approximately 15 ns before the peak. In order to get the peak of the signal and estimate its uncertainty the fit parameters from the polynomial were smeared according to their uncertainties. The function which was fitted to the test pulse shapes was

$$f(t) = A_0 + A_1 t + A_2 t^2 + A_3 t^3 + A_4 t^4 + A_5 t^5 + A_6 t^6 \quad (2)$$

where f is the pulse amplitude and t is the time in nanoseconds. Table 4 shows the values of the polynomial parameters and their fractional uncertainties.

The overspill fraction was estimated using the fitted 6th order polynomial given in Equation 2. This overspill was calculated using

$$Overspill = \frac{f(t_{overspill})}{f(t_{peak})}, \quad (3)$$

where $f(t_{peak})$ is the peak amplitude and $f(t_{overspill})$ is the overspill amplitude with $t_{overspill} = t_{peak} + 25ns$. The overspill uncertainty is also obtained smearing the polynomial fit parameters.

The undershoot was calculated using a similar approach as for the overspill calculation. The only difference is that the pulse amplitude on the undershoot region is parametrised as a 6th polynomial fitted on the time range between 80 and 140 ns. The minimum value of this fitted polynomial gives the undershoot amplitude. On both the R and the Φ-sensors it was estimated to be of the order of 17% with respect to the signal peak. This number was calculated for all configurations of the Beetle parameters tested.

The signal peak and the overspill were calculated using the tested n^+-in-n module and n^+-in-p module using the range of Beetle parameters settings and on both R and Φ-sensors. Figures 29, 30, 31 and 32 show the signal and overspill as a function of the Beetle parameters for both types of VELO modules and for both sides of the hybrid.

Table 4: List of fit parameters, P, and the absolute value of the ratio between the associated errors and the parameters.

Parameter number	Parameter Value	$\lvert\delta P/P\rvert$
A_0	-3.53 $\times$ 10^{2}	4.1$\times$ 10^{-3}
A_1	2.39 $\times$ 10^{1}	1.8$\times$ 10^{-3}
A_2	-4.48 $\times$ 10^{0}	1.2$\times$ 10^{-3}
A_3	1.60 $\times$ 10^{-3}	4.2$\times$ 10^{-3}
A_4	3.39 $\times$ 10^{-5}	2.3$\times$ 10^{-3}
A_5	-3.53 $\times$ 10^{-7}	2.3$\times$ 10^{-3}
A_6	9.71 $\times$ 10^{-10}	7.5$\times$ 10^{-4}

The signal peak was measured to be higher for most of the Beetle parameters that were tested on the n^+-in-p module compared to the n^+-in-n module. The difference between the overspill estimates of the two types of modules was small. The estimated overspill for both technologies were quite similar - only a few percent higher with the n^+-in-p technology in most of the values set for the chip parameters.

The observed increase of the signal peak with the increase in the V_{fs} parameter was about 3 ADC units for both n^+-in-n and n^+-in-p modules and on both sides (R and Φ-hybrids). On the R-side the overspill increased by about 9 % on the n^+-in-n module and by about 13 % on the n^+-in-p module. On the Φ-side the overspill change was 11 % and 10 % respectively. The uncertainty on these variations was estimated to be $\pm$4 %. No significant change in the signal and overspill was observed for the different tested values of V_{fp}, I_{pre} and I_{sha}. The obtained variations agree with those obtained in [14] which studied Beetle parameter settings on a 300 μm R-measuring VELO proto-type module.

The peak of the pulse and the overspill were also calculated as a function of the strip length of the R-sensors using the default Beetle parameter settings. Figure 33 shows the test pulse peak and overspill calculated for as a function of strip length for both the n^+-in-n and n^+-in-p modules. The length of the strips were calculated using the VELO Detector Element package which provided a geometric description of the active area of the sensors [15]. The radius and Φ-angle of the strips was obtained via the DeVeloRType class as a function of the strip number. Hence the length of the strips was obtained as the product of the radius and the Φ-angle of the strip. The association between the chip channels and the strips numbers was also available via a method within this class. The peak amplitude was approximately constant across the range of strip lengths (4 mm - 34 mm) for both the n^+-in-n and n^+-in-p modules. As already discussed, the n^+-in-p module had slightly higher ADC values compared to the n^+-in-n module for almost all strip lengths. The overspill was approximately 30% for both the n^+-in-n and n^+-in-p modules for all measured strip lengths.

Figure 34 shows the ratio as a percentage of the pulse amplitude as a function of time and the pulse peak for the n^+-in-n module. It was calculated in steps of 25 ns after the pulse peak and for all Beetle chip parameters tested. Full restoration of the signal was still not achieved after 180 ns for all of the parameters which were tested . V_{fp} was seen to have an affect on the overspill and undershoot regions, where the maximum undershoot was reduced as V_{fp} was increased. V_{fs} was also seen to reduce the maximum undershoot

as V_{fs} was reduced, although no effect on the rise time and peak signal was measured. The rise time and fall time of the signal was seen to reduce and the maximum undershoot was increased as I_{pre} was increased. Finally, the shaper amplifier bias current, I_{sha}, reduced the rise time and reduced the maximum undershoot as the settings were increased from 80 to 150 μA.

11 Bad Channels Analysis

The aim of analysing the electronic data from the burn-in for each channel on the sensors was to identify any new problematic channels and to determine if any extra problem had occurred during burn-in. This information was also cross-checked against the Liverpool test list to see if any new problems had occurred. The list of bad channels combined observations from bond inspections made during the visual inspection of the modules and the noise measurements made during the electronic data taking. As mentioned previously in Section 5, the visual inspection identified non-bonded or shorted channels. During the electrical measurements noisy and dead channels were found by applying specified cuts on the estimated noise depending on the corresponding strip position. The analysis resulted in a list of bad channels which are compared to the list of bad channels that were compiled from laser tests in Liverpool University.

11.1 Liverpool Classifications

The first list of bad channels was compiled during the module assembly phase at Liverpool University. A high-resolution visual inspection, laser scan and noise analysis were performed in order to uncover the possible problems that could cause channels to have a bad performance. These tests provided information on the physical integrity of the channels and their actual functionality.

The bad channels were classified into five categories according to the different results obtained from the three procedures in Liverpool University. The channel categories are listed as:

- Dead channels which were usually identified though the laser scan when the measured signal was too low or when the raw noise was low;
- Noisy channels which were defined to be when the readout channels had a noise higher than the usual limits.
- Low Gain channels were identified by the laser scan and were defined as occurring when the signal amplitude was below the expected values.
- Open channels occurred when the Front-End Bond or the Sensor-End Bond was not connected.
- Short channels occurred when the channel was connected to another channel in its vicinity. These were identified by charge sharing during the laser tests or through the high resolution visual inspections.

Table 5: Rejection criteria for bad strips on the R and Φ-sensors

Cut	R	Φ (inner)	Φ (outer)
Raw Noise [ADC]	< 1.5	< 1.5	< 1.5
CMS noise [ADC]	> 2.7	> 2.7	> 2.7
⟨RawNoise⟩ - Raw Noise [ADC]	< 0.4	< 0.45	< 0.65
CMS Noise - ⟨CMSNoise⟩ [ADC]	> 0.5	> 0.45	> 0.45

11.2 Burn-in Electrical Tests

The noise analysis procedure was performed on both of the R and Φ-sensors and the procedure was similar for both sensors. The same set of variables was used and only the values of the applied cuts differed slightly from one sensor type to the other. Different values of ADC cuts were also applied if the strip was in the inner region or the outer region of the Φ-sensors.

The noise for each channel was calculated with the raw data and with the common mode suppressed data. A channel was considered dead if its raw noise was below a minimum limit or it was classified as noisy if the common mode suppressed noise is above a maximum limit.

Each channel also had its raw noise and common mode suppressed noise compared to the average noise obtained over all channels in its link.

The applied cut on the raw noise was calculated as the average raw noise in the link subtracted from the measured raw noise. If the raw noise was below this value it was classified as a dead channel i.e. if the raw noise on the R-sensor was more than 40 % below the average noise for that link it was defined as dead. The cut on the common mode corrected noise was calculated as a fixed factor of the average common mode suppressed noise in the link and the channel was classified as noisy if it was above this value. The values of the cuts used for different sensors and regions are listed in Table 5. There was an additional cut for the outer strips of the Φ-sensor which were overlaid by a routing line. The noise cut on these strips was increased by 0.2 ADC counts.

Three different quantities were estimated in order to provide comparison figures between the VELO sensors. The first of the three quantities was the absolute number of bad channels. The second calculated quantity was the ratio between the number of new bad channels found in the burn-in since the Liverpool measurements and the number of channels found in agreement with Liverpool and the burn-in bad channels lists. The third quantity was the ratio between the number of channels categorized as bad in Liverpool but were not identified as bad in the burn-in analysis and the number of channels in agreement with Liverpool and burn-in. Figure 35 shows these three quantities as a function of the module number for both R and Φ-sensors.

Figure 35 shows that the total number of bad channels on the R-sensors was less than 35 for all sensors (equivalent to less than 1.7 % bad channels) and less than 21 bad channels for all Φ-sensors (equivalent to less than 1.0 % bad channels). Almost all of the new bad channels found in the burn-in were typically on the edge of the cuts. On the other hand the cuts used were crudely optimised to reject as many genuine problem channels while not enforcing too tight cuts so that good channels were rejected. The total number of

Table 6: The total number of bad channels found in Liverpool University and the burn-in laboratory, the number of channels in agreement between the two bad channels lists, the percentage of the number of new bad channels compared to the channels in agreement and the percentage of the number of selected bad channels in Liverpool that were not rejected by cuts on the electrical data analysis in the burn-in laboratory compared to the channels in agreement.

	$\text{Total}_{Burn-in}$	$\text{Total}_{Liverpool}$	Agreement	$\frac{\text{New}}{\text{Agreement}}$	$\frac{\text{Not Rejected}}{\text{Agreement}}$
R	451	435	328	0.37	0.18
Φ	342	336	278	0.29	0.39

bad channels found in Liverpool and in the burn-in were respectively 435 and 451 on the R-sensor and 336 and 342 on the Φ-sensors. An overall agreement of 79% with Liverpool bad strips list has been found for the combined results of the R and Φ-sensors. Table 6 shows the total number of bad channels found in Liverpool University and the burn-in laboratory, the number of channels in agreement between the two bad channels lists, the percentage of the number of new bad channels compared to the channels in agreement and the percentage of the number of selected bad channels in Liverpool that were not rejected by cuts on the electrical data analysis in the burn-in laboratory compared to the channels in agreement.

Table 6 shows that the total number of bad channels that were found was higher for both sensor types compared to the lists compiled in Liverpool University. Most of the differences were due to the cuts that were applied and in hindsight, the cuts applied in the burn-in could have been slightly tighter to allow for more of an agreement with the bad channel list compiled in Liverpool University.

According to numbers obtained on the burn-in analysis the mean number of bad strips per module was estimated to be 14 on the R-sensors and 10 on the Φ-sensors. An uncertainty of 20% on the number of bad strips was estimated by varying the cuts applied on the analysis selection. Therefore the average percentage of problem strips in the whole VELO was measured to be $0.7\pm0.1\%$ for the R-sensors and $0.5\pm0.1\%$ for the Φ-sensors. The number of channels which were measured to be shorted were 60 in total for all R-sensors measured and 51 channels for all Φ-sensors[4], which was equivalent to 13% and 15% of the total number of bad channels found in the R and Φ-sensors in the burn-in laboratory tests. If the shorted channels were used they would result in a degraded resolution performance however, these channels form a significant proportion of the total bad channels measured and perhaps they could be used in the future operation of the VELO.

12 Conclusions

The VELO modules have been extensively tested in the burn-in laboratory. The testing rate successfully managed to follow the production delivery rate and the module

[4] Two channels that were shorted together counted as two

assembly rate. A few problem features on the modules were picked up during the detailed visual inspections and the results were fed back into the Liverpool University production, such as an early problem with a vacuum holding jig which was deforming the high voltage return bonds on early production modules.

Six of the 42 production modules were thermally imaged before and after the electrical and thermal burn-in tests and all of the images showed no problems on the front end chips or areas of non-uniformity. Throughout the electrical tests the signal to noise ratio was calculated from the header and the ratio was monitored and no problems were found.

The leakage current of the sensors were carefully measured and compared throughout the personal history of each module. Only a few of the Φ-sensors were found to suffer from a thermally induced increase in leakage current and only one of these modules was withheld from production as a spare. No correlation was found between the metrology performed in Liverpool University and the leakage current of the sensors. The majority of the high leakage current sensors were Φ-sensors and it was found that most of these high leakage current Φ-sensors originated from wafer position *A* which was near the edge of the wafer.

The Beetle parameters were scanned and compared for an n^+-in-n VELO module and an n^+-in-p module. The results from the scans were similar to scans performed for previous versions of the VELO hybrid and the behaviour of the n^+-in-n and n^+-in-p modules were not dissimilar. The bad channels were analysed using information from both the visual inspections and the electrical tests. The agreement between the list of bad channels found in Liverpool University and the burn-in laboratory was good. Overall there were 0.7% and 0.5% bad channels measured in the burn-in laboratory on the R and Φ-sensors respectively.

The overall performance of the VELO modules were excellent. There were very few problems discovered during the burn-in testing. The testing performed in the burn-in has enriched the confidence which the VELO detector can be operated.

Acknowledgements The authors would like to thank all the VELO group for their considerable input - special thanks to Paula Collins, Raphael Dumps, Doris Eckstein, Kazu Akyiba, Jan Buytaert, Marco Gersabeck, Richard Jacobsson and many more. The Liverpool LHCb group have been especially helpful, in particular we would like to thank Themis Bowcock, Girish Patel, Tony Affolder and Tony Smith.

References

[1] A. Bates *et. al*, A setup for testing the LHCb VELO modules, LHCb 2007-102 VELO, July 2007.

[2] VELO Module Burn-in, Links to the daily elog, presentations and documentations concerning the Glasgow burn-in of LHCb VELO modules, http://ppewww.physics.gla.ac.uk/LHCb/Velo_Burn/lhcb_velo_burn-in.html, Last edited on 03/05/07.

[3] LHCb Vertex Locator Technical Design Report, CERN/LHCC 2001-011

[4] Lochner S. & Schmelling, The Beetle Reference Manual, LHCb-2005-105 ELETRONICS, August 22, 2006

[5] LHCb VELO Assembly Twiki pages, https://twiki.cern.ch/twiki/bin/view/LHCb/VELOAssembly, last editted on 05/03/07.

[6] R. Mountain, VELO module transport box reference document and operational guide, Syracuse University note, SU-LHCb Note, 2006-03-02.

[7] Liverpool University LHCb VELO module database, http://velodb.ph.liv.ac.uk/lhcb/index.html, April 2007.

[8] R. Jacobsson, ODIN Raw Data Format, Feb 2006, CERN EDMS 704084-v1.2, http://lhcb-online.web.cern.ch/lhcb-online/TFC/documents/ODIN_rawdata_edms704084_1.pdf.

[9] R. Jacobsson *et. al*, The LHCb Timing and Fast Control System, R. Jacobsson et al., LHC Electronics Workshop, 2001, http://lhcb-online.web.cern.ch/lhcb-online/TFC/documents/LEB2001_paper.pdf.

[10] G. Haefeli *et. al*, The LHCb DAQ interface board TELL1, NIM A 560 (2006) 494-502.

[11] R. Frei, Documents prepared for the VELO Electronics Production Readiness Review, Repeater motherboard, low voltage and driver cards, 16th January 2006, link to agenda page http://indico.cern.ch/conferenceDisplay.py?confId=a058471.

[12] T. Szumlak, VELO ACDC Software training, Vetra tutorial, 27th June 2006, CERN, http://indico.cern.ch/conferenceDisplay.py?confId=4076.

[13] L. Eklund, M Pivk, J. Buytaert, P. Collins, D. Eckstein, J.P. Palacios, Absolute calibration of Beetle1.3 test-pulse, noise and header using MIP signals from an ATLAS reference detector, LHCb-2004-068 VELO, January 10, 2005.

[14] J.P. Palacios *et al.*, Pulseshape characteristics of a 300 μm PR03 R-measuring VELO sensor read out with a beetle 1.3 chip, LHCb-2004-068 VELO,January 10, 2005.

[15] The VELO Detector Element, http://mtobin.home.cern.ch/mtobin/LHCb/VeloDet.html

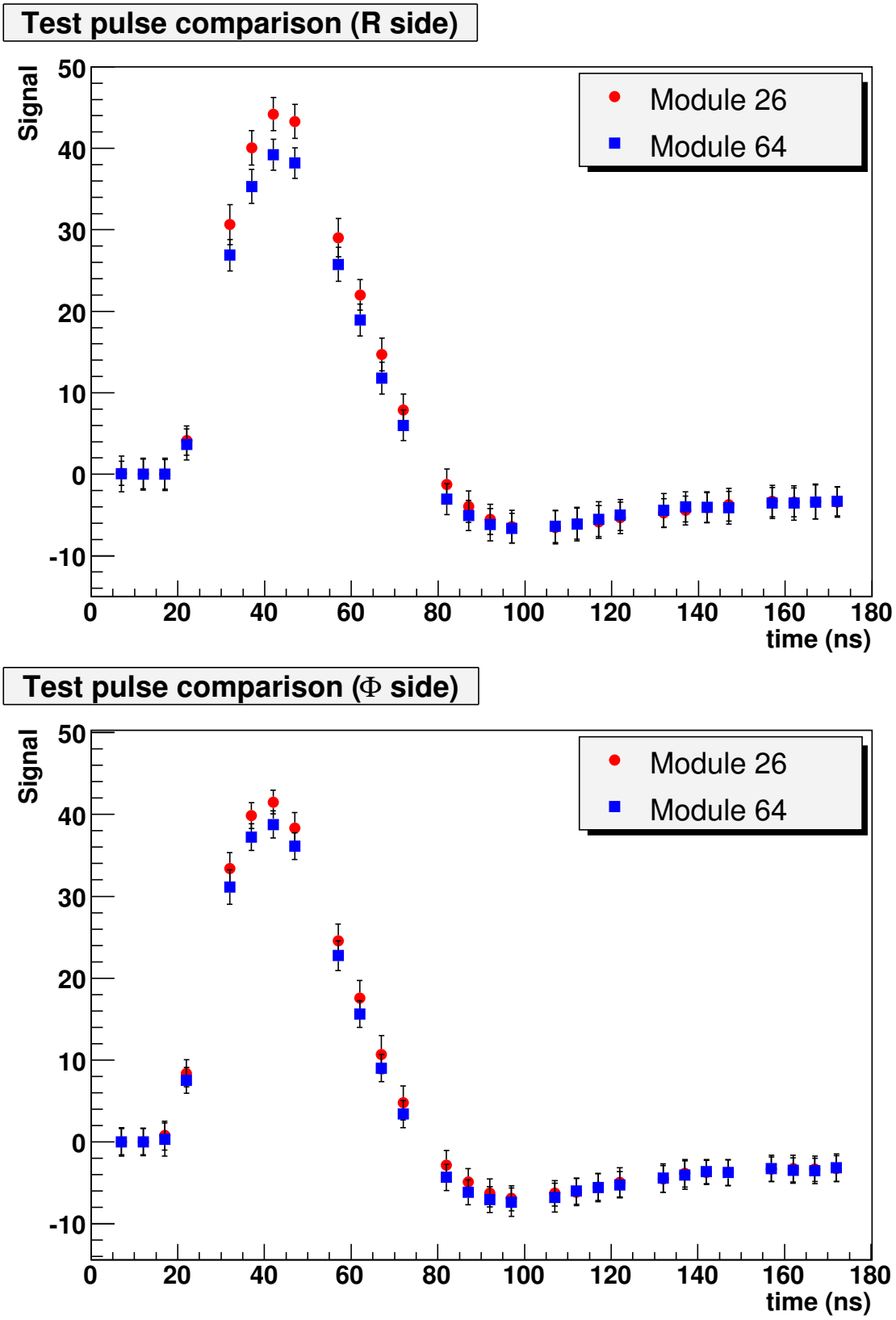

Figure 24: The signal measured in response to test pulses in the Beetle chips using the default Beetle parameters. The red circular markers correspond to the n^+-in-p module and the blue square markers correspond to the n^+-in-n module. The top plot compares the R-sides from the two tested modules and the bottom plot compares the Φ-sides from the two tested modules.

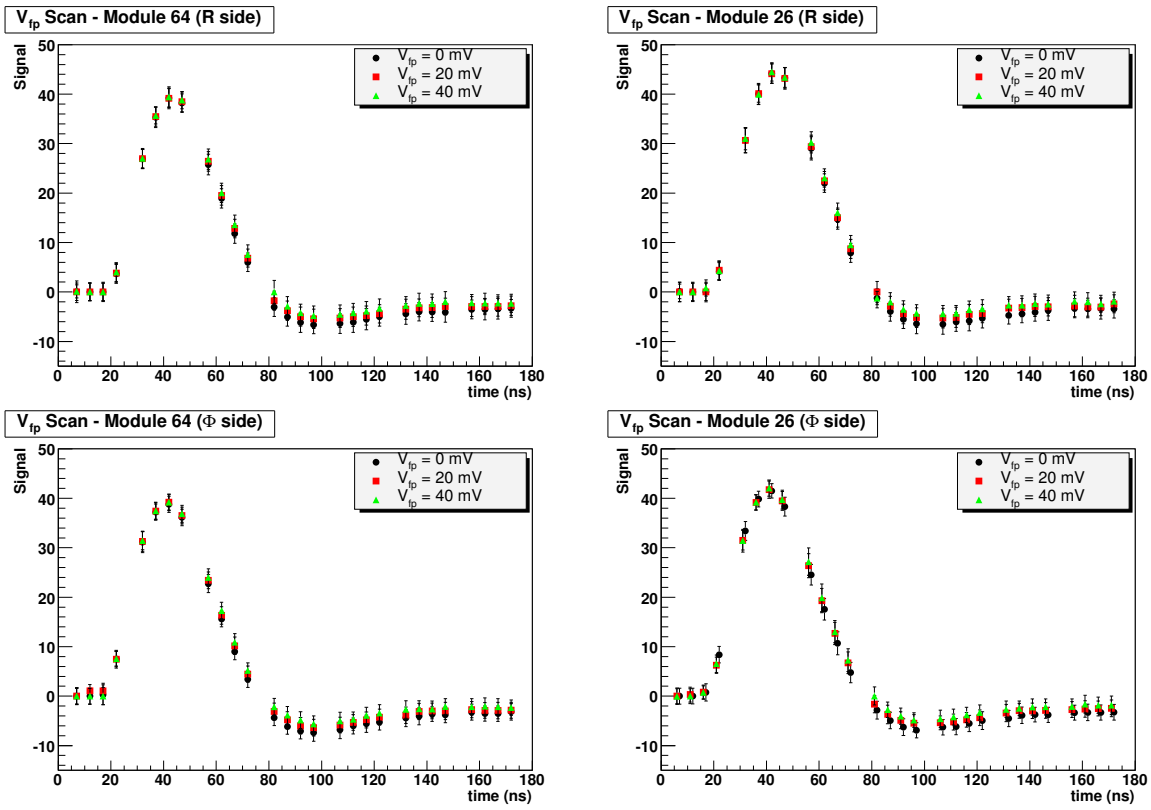

Figure 25: Pulse shapes for different values of V_{fp}. The top two plots show the measured signal for the R side and the bottom two plots show the measured signal for the Φ side. The plots in the left column show the measured signal for the n^+-in-n module (module 64) and the measured signal for the n^+-in-p module (module 26) are shown in the plots on the right column.

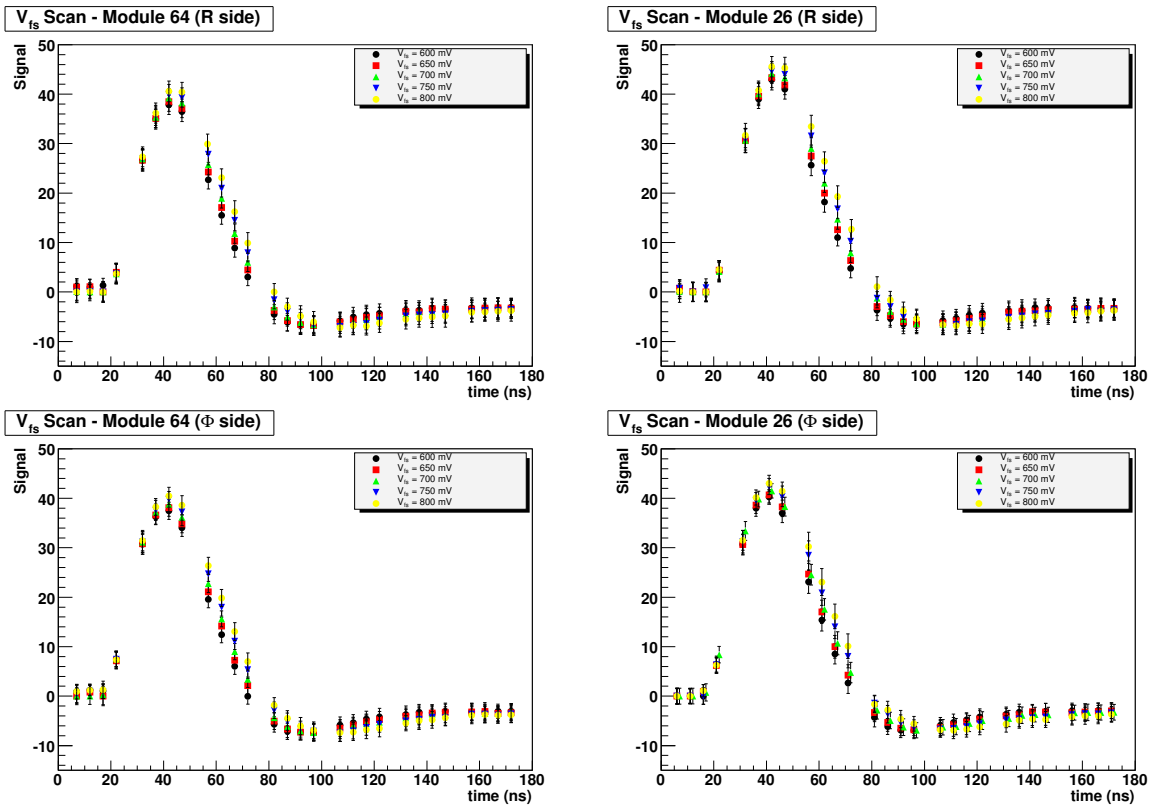

Figure 26: Pulse shapes for different values of V_{fs}. The top two plots show the measured signal for the R side and the bottom two plots show the measured signal for the Φ side. The plots in the left column show the measured signal for the n^+-in-n module (module 64) and the measured signal for the n^+-in-p module (module 26) are shown in the plots on the right column.

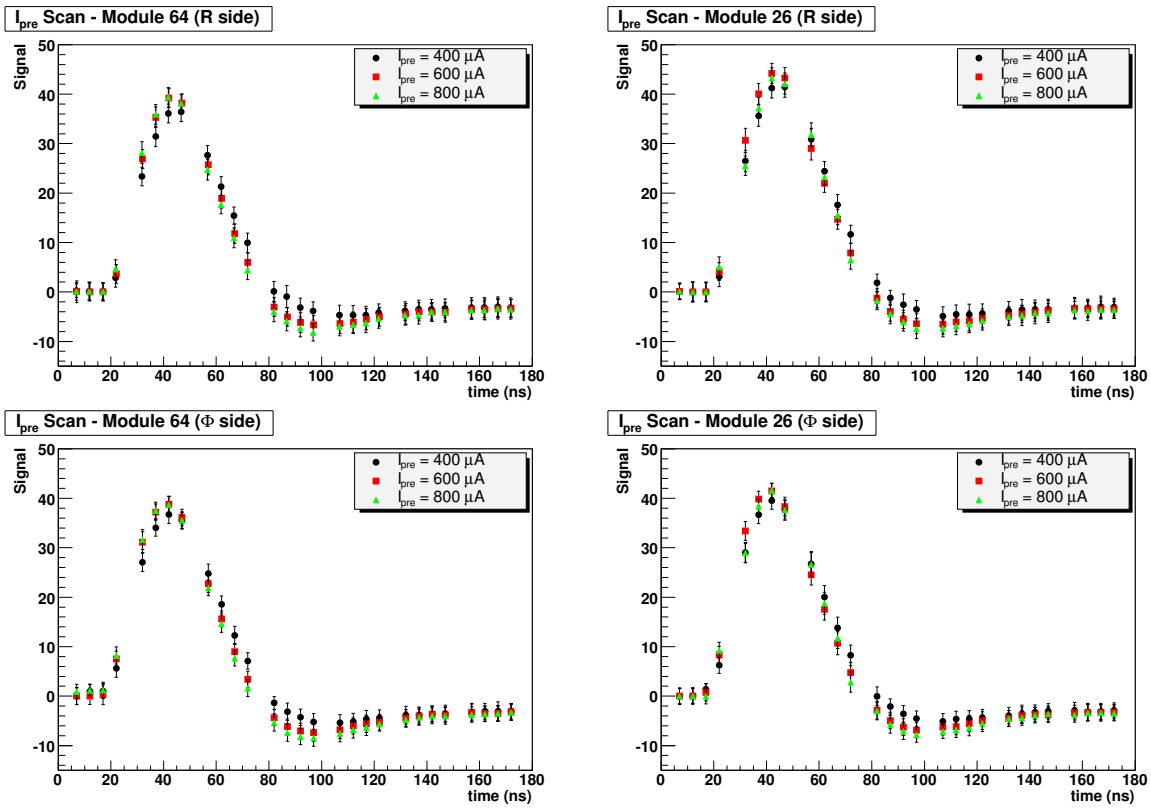

Figure 27: Pulse shapes for different values of I_{pre}. The top two plots show the measured signal for the R side and the bottom two plots show the measured signal for the Φ side. The plots in the left column show the measured signal for the n^+-in-n module (module 64) and the measured signal for the n^+-in-p module (module 26) are shown in the plots on the right column.

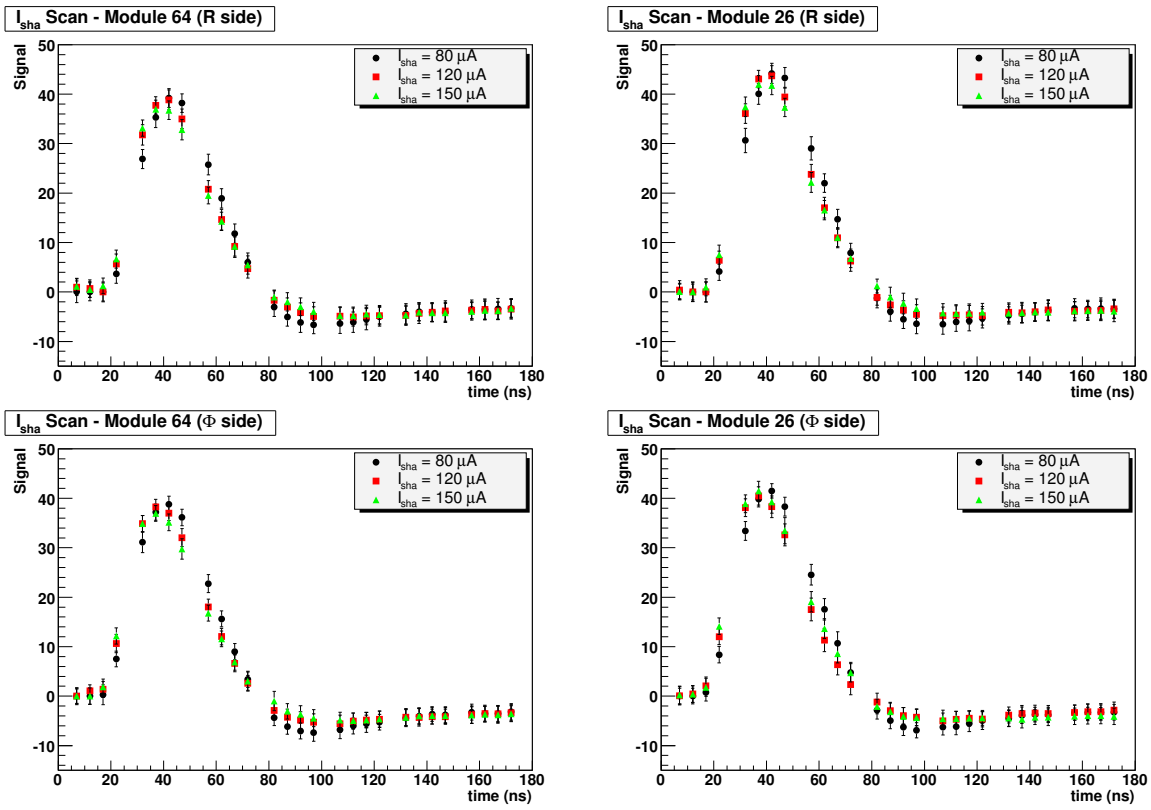

Figure 28: Pulse shapes for different values of I_{sha}. The top two plots show the measured signal for the R side and the bottom two plots show the measured signal for the Φ side. The plots in the left column show the measured signal for the n^+-in-n module (module 64) and the measured signal for the n^+-in-p module (module 26) are shown in the plots on the right column.

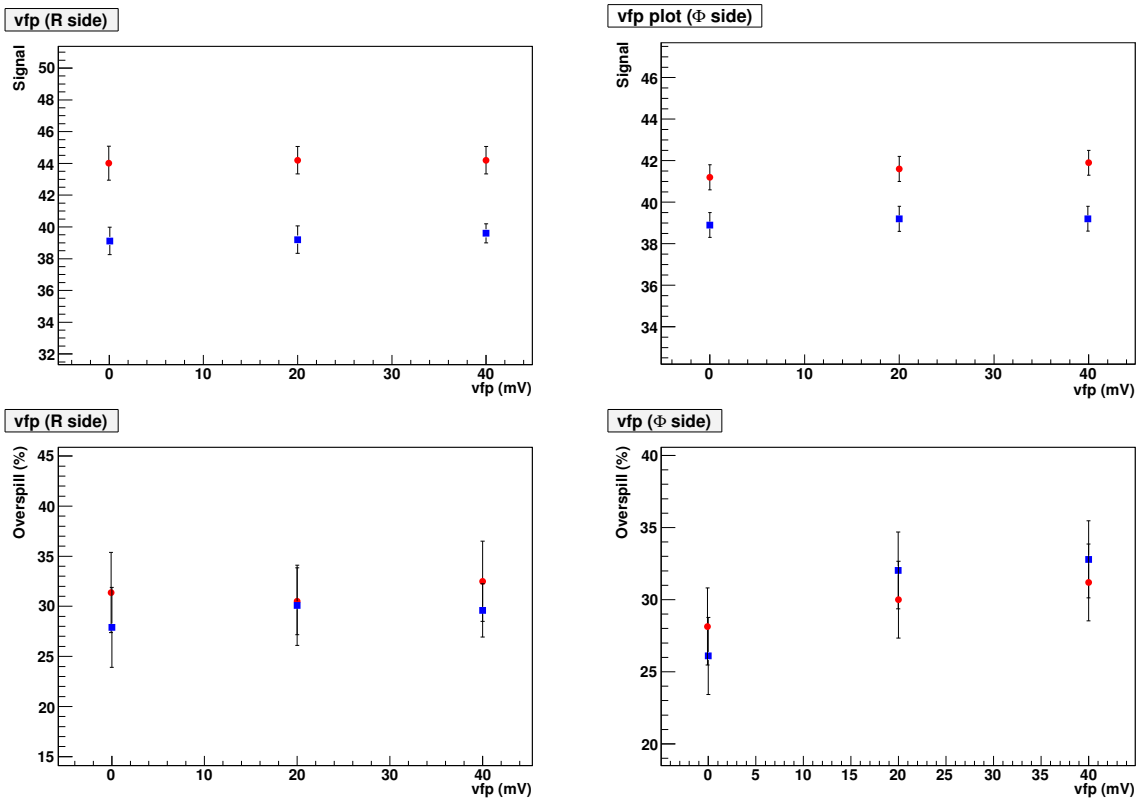

Figure 29: The top (bottom) two plots show the measured signal (overspill) from Beetle test pulses as a a function of V_{fp} on both the R and the Φ-sides of the module. The red circle markers correspond to the n^+-in-p modules and the blue square markers correspond to the n^+-in-n module.

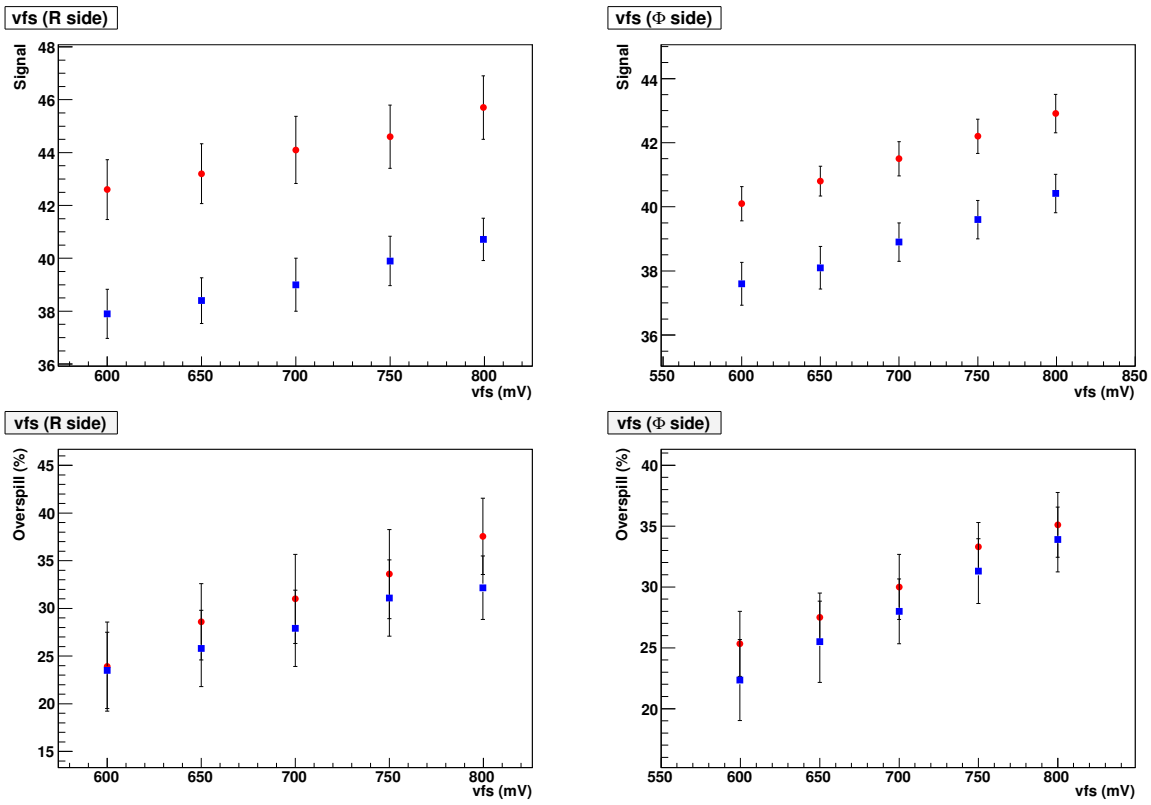

Figure 30: The top (bottom) two plots show the measured signal (overspill) from Beetle test pulses as a a function of V_{fs} on both the R and the Φ-sides of the module. The red circle markers correspond to the n^+-in-p modules and the blue square markers correspond to the n^+-in-n module.

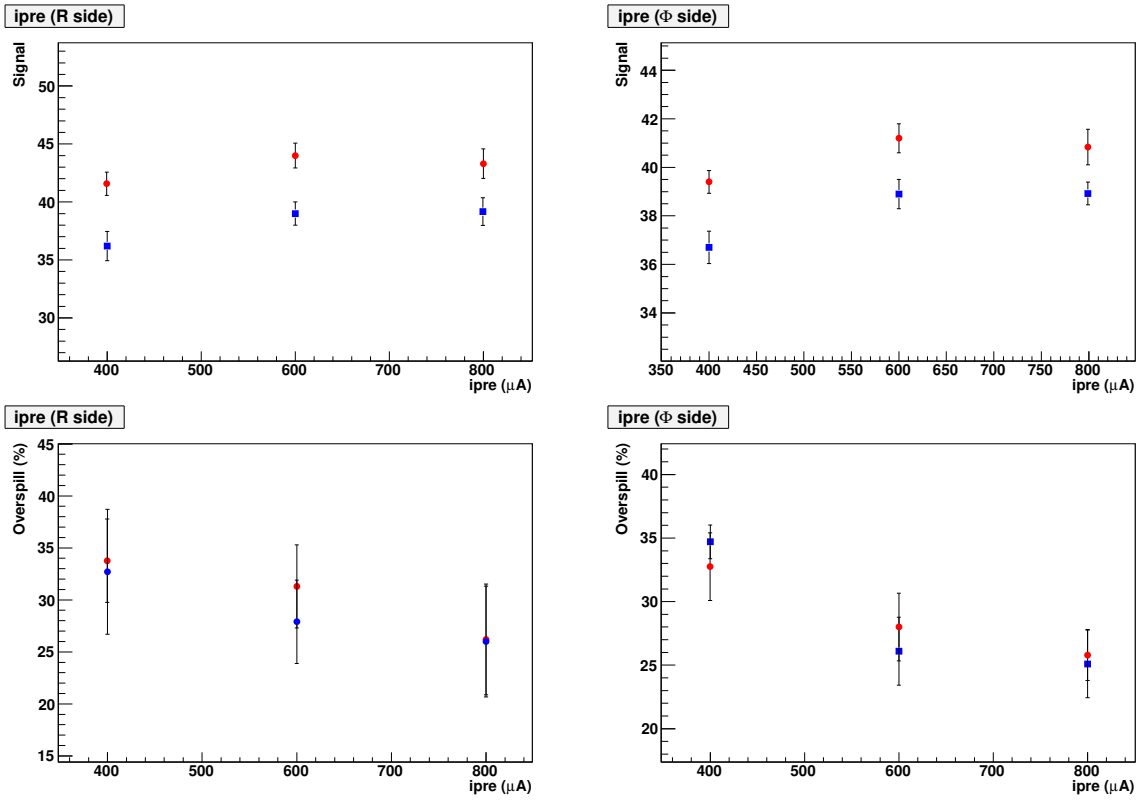

Figure 31: The top (bottom) two plots show the measured signal (overspill) from Beetle test pulses as a a function of I_{pre} on both the R and the Φ-sides of the module. The red circle markers correspond to the n^+-in-p modules and the blue square markers correspond to the n^+-in-n module.

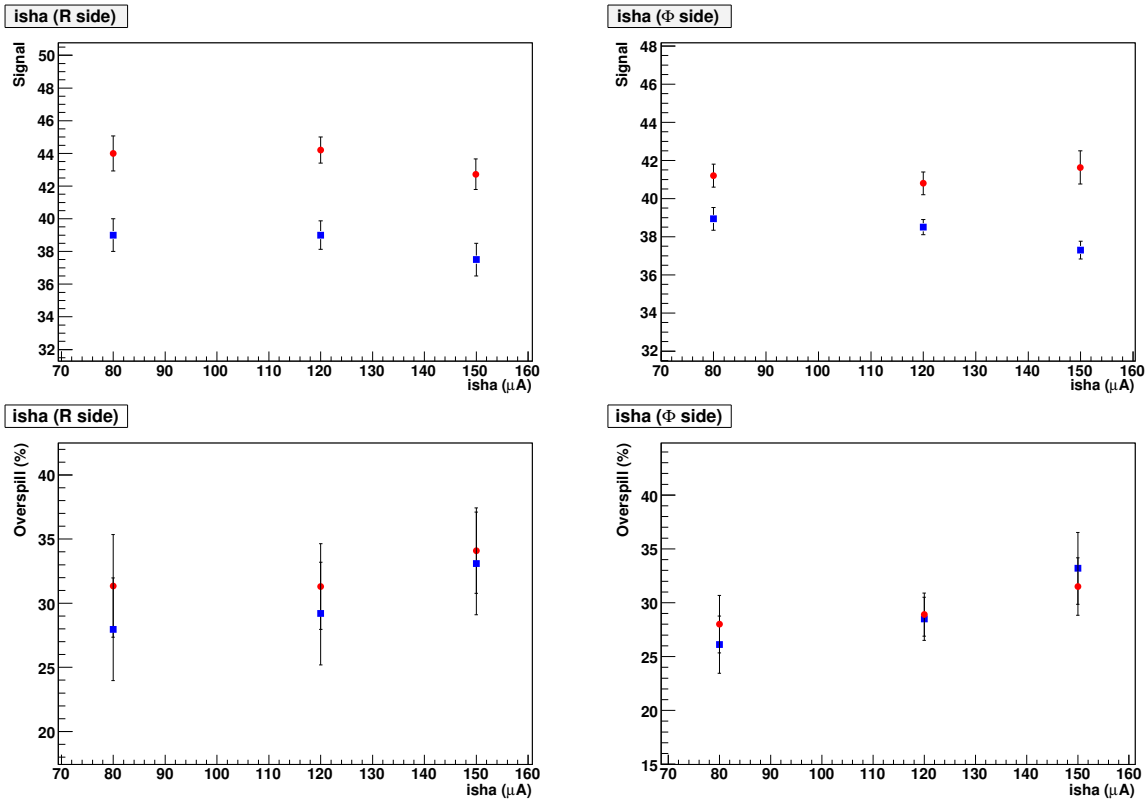

Figure 32: The top (bottom) two plots show the measured signal (overspill) from Beetle test pulses as a a function of I_{sha} on both the R and the Φ-sides of the module. The red circle markers correspond to the n^+-in-p modules and the blue square markers correspond to the n^+-in-n module.

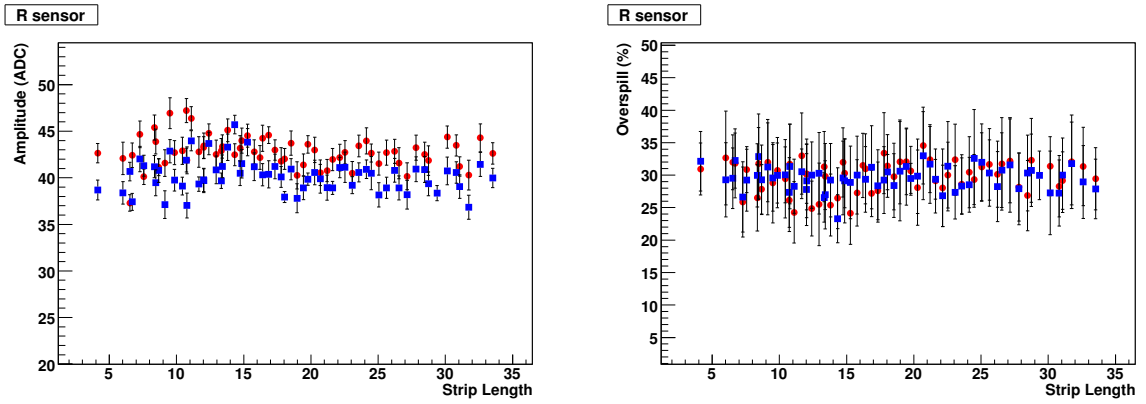

Figure 33: Test pulse peak (left) and overspill (right) as a function of the strips length in millimetres on R-sensors. The blue square markers are the values calculated for the n^+-in-n module and red circular markers are the values calculated for the n^+-in-p module. The default Beetle parameters were used.

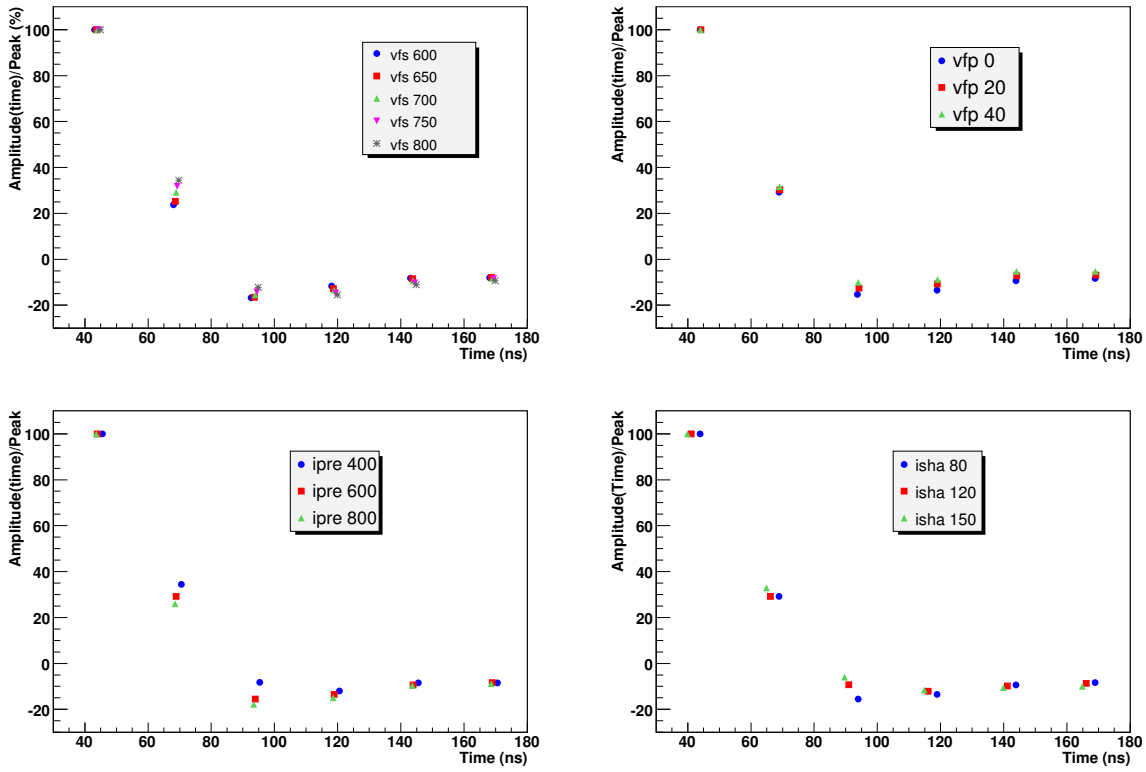

Figure 34: The ratio between the pulse amplitude as a function of the time and the pulse peak expressed as a percentage. The top left plot used the default Beetle parameters for V_{fp}, I_{pre} and I_{sha} and varied the V_{fs} parameter, where the tested values for V_{fs} are shown in the legend. The other 3 plots had the same format, where the parameter in the legend was varied and the default Beetle settings were used for the other 3 parameters.

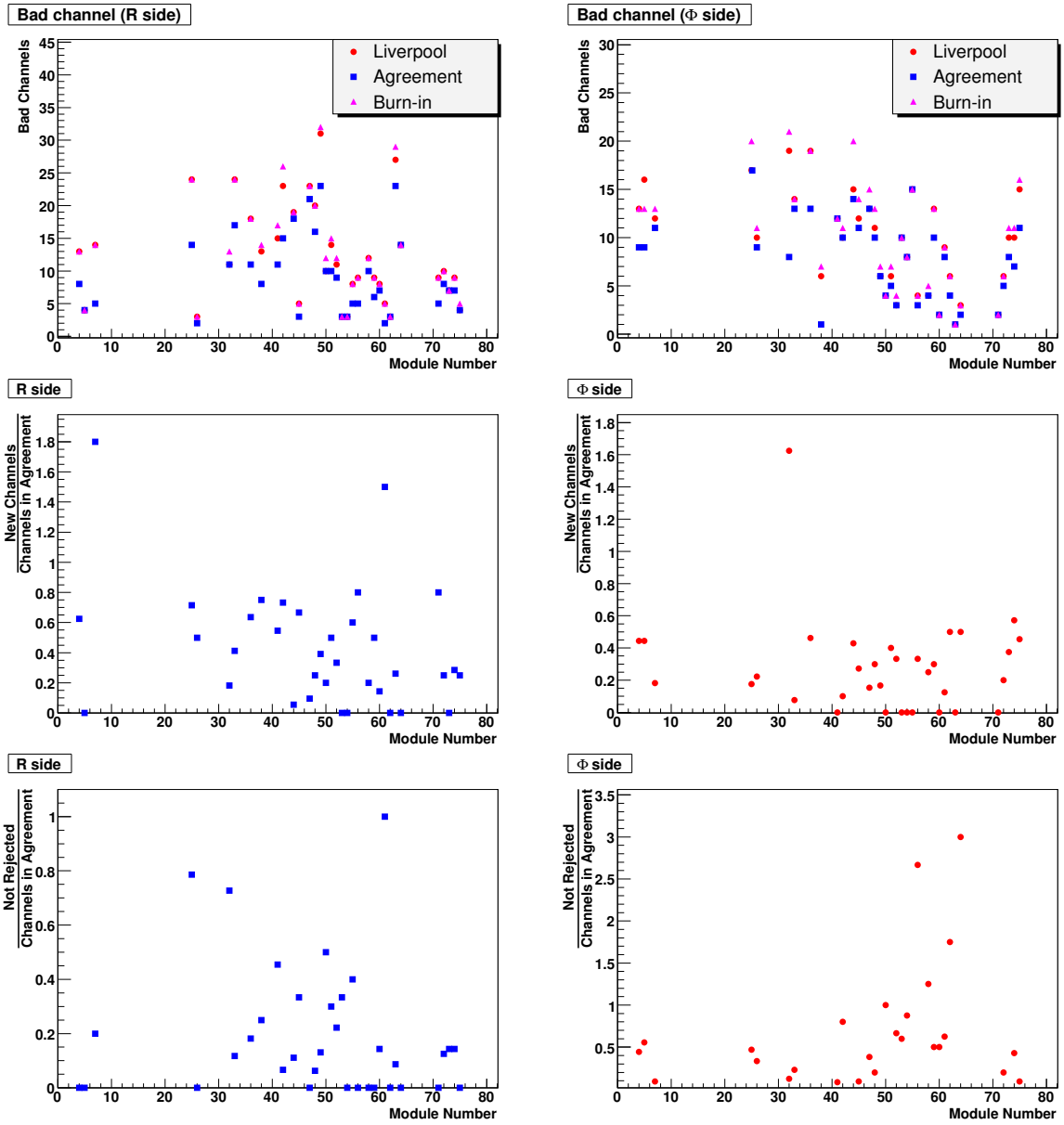

Figure 35: Top row: The number of bad channels as a function of the module number for both the R (left plot) and the Φ-sensors (right plot). The red circle markers are the bad channels classified in Liverpool, the purple triangle markers are the bad channels found in the burn-in laboratory and the blue square markers are the number of bad channels that were in agreement. Centre row: The ratio between the number of new problematic channels found in the burn-in and the number of channels found in agreement with Liverpool on the R (left) and Φ-sensors (right). Bottom row: The ratio between the number of channels categorised as bad in Liverpool but not rejected in the burn-in analysis and the number of channels in agreement with Liverpool on the R (left) and Φ-sensors (right).